Rock stresses

Author: Prof. Dr. habil. Heinz Konietzky
(TU Bergakademie Freiberg, Geotechnical Institute)

Editor: Prof. Dr.-Ing. habil. Heinz Konietzky Layout: Alexandra Morgenstern
TU Bergakademie Freiberg, Institut für Geotechnik, Gustav-Zeuner-Straße 1, 09599 Freiberg • sekr_fm@ifgt.tu-freiberg.de

1 Introduction

The virgin stress state (primary stress state) in the earth's crust is predominantly produced or influenced by the following components:

- Tectonic forces (plate tectonics)
- Gravitational forces
- Topography
- Residual stresses (e.g. overconsolidation)
- Thermal stresses
- Induced stresses due to inhomogeneities and anisotropies
- Swelling pressures
- Water pressures

The stress field can be described by the stress tensor:

$$\sigma_{ij} = \begin{bmatrix} \sigma_{11} & \sigma_{12} & \sigma_{13} \\ \sigma_{21} & \sigma_{22} & \sigma_{23} \\ \sigma_{31} & \sigma_{32} & \sigma_{33} \end{bmatrix} = \begin{bmatrix} \sigma_{xx} & \sigma_{xy} & \sigma_{xz} \\ \sigma_{yx} & \sigma_{yy} & \sigma_{yz} \\ \sigma_{zx} & \sigma_{zy} & \sigma_{zz} \end{bmatrix},$$

where identical indices indicate normal stresses and unequal indices shear stresses. The stress tensor is a second rank tensor, which can be transformed into the main axis system, where shear stresses vanish and normal stresses reach extreme values:

$$\sigma_{ij} = \begin{bmatrix} \sigma_1 & 0 & 0 \\ 0 & \sigma_2 & 0 \\ 0 & 0 & \sigma_3 \end{bmatrix}.$$

σ_1, σ_2 and σ_3 are called principal stresses. Therefore, the complete stress state is given by either the 9 or 6 (in case of equivalent shear stresses according to the Boltzmann axiom) elements of the stress tensor or the 3 principal stresses and the corresponding orientations (Fig. 1).

Often, in a simplified manner the stress field is expressed by a vertical principal stress component (*SV*) and quasi-horizontal major (*SH*) and minor (*Sh*) principal stress components. In most cases, at least at greater depths, the vertical stress component corresponds to the overburden weight of the overlying rock masses:

$$SV = \rho g h$$

2 Results of field measurements

More general and large-scale trends of stresses in the earth's crust can be obtained by consulting the World-Stress-Map (WSM 2014). The WSM is a database, which contains in-situ stress measurements obtained by quite different methods and allows the determination of large-scale stress regimes according to definitions given in Fig. 2.1. Exemplary, Fig. 2.3 and 2.4 show the orientation of maximum principal stress component and corresponding stress regimes (normal faulting, strike slip and thrust faulting) for Europe and Germany.

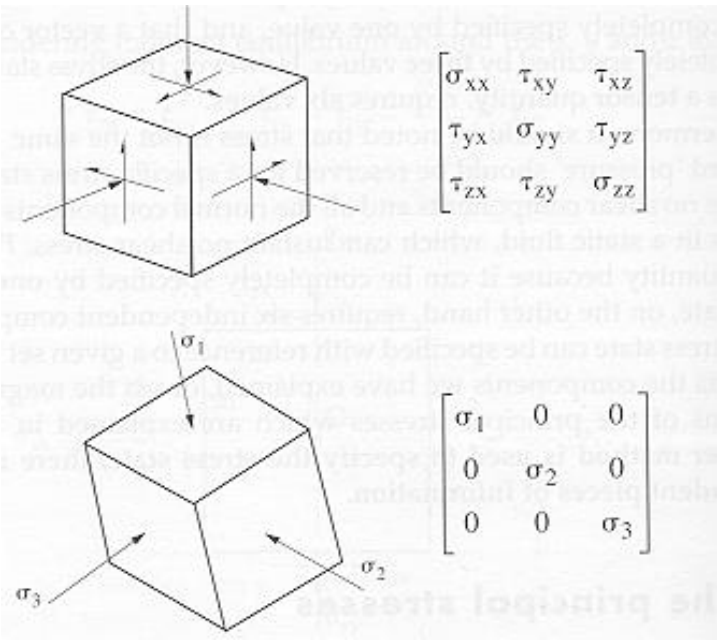

Fig. 2.1: Definition of stress tensor

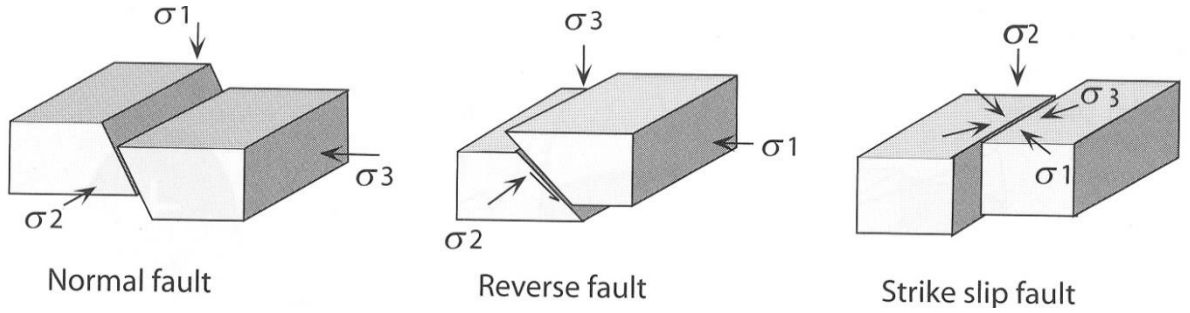

Fig. 2.2: Illustration of stress regimes

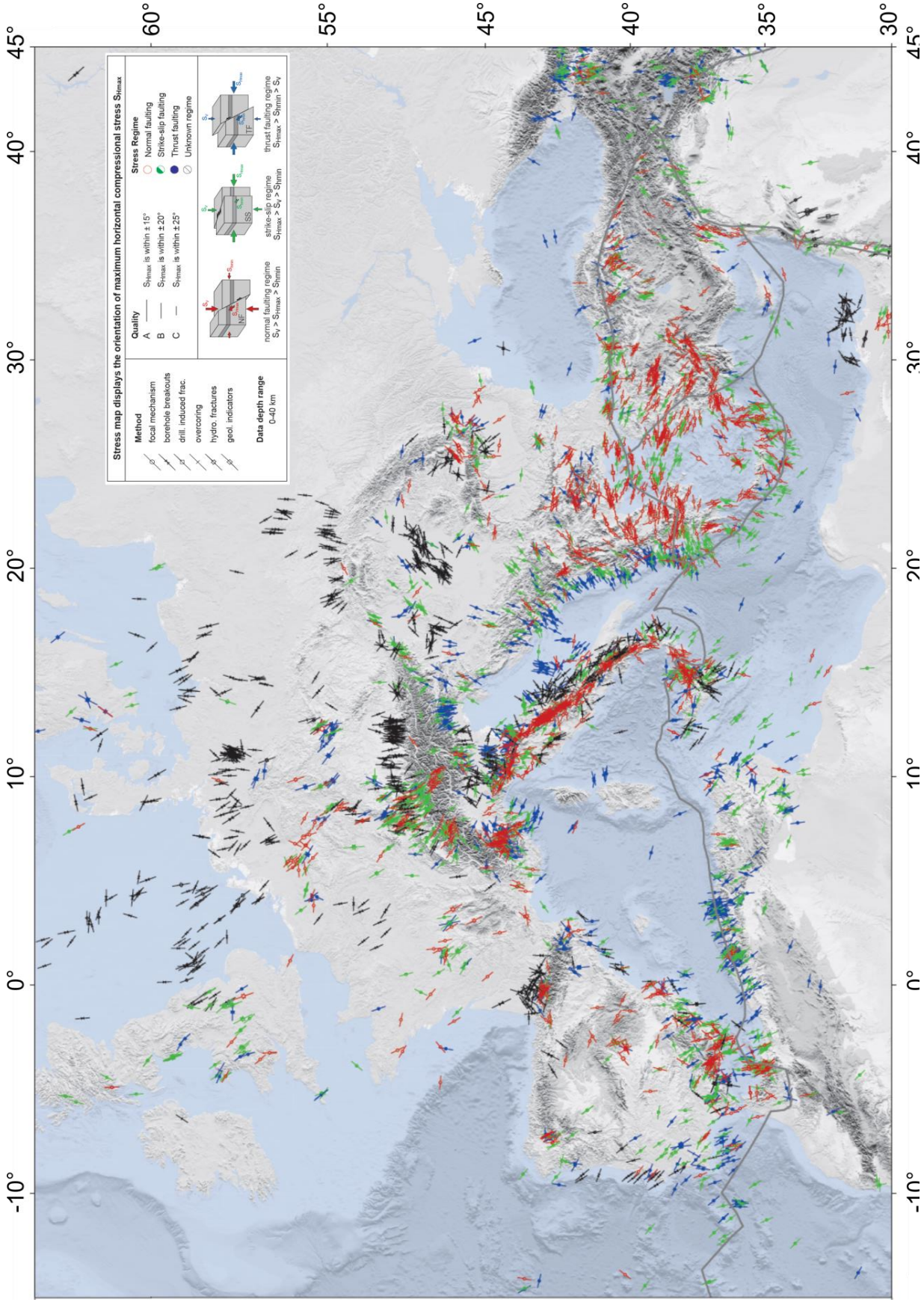

Fig. 2.3: Maximum principal stress orientation and stress regimes for Europe (modified after Heidbach et al. 2016)

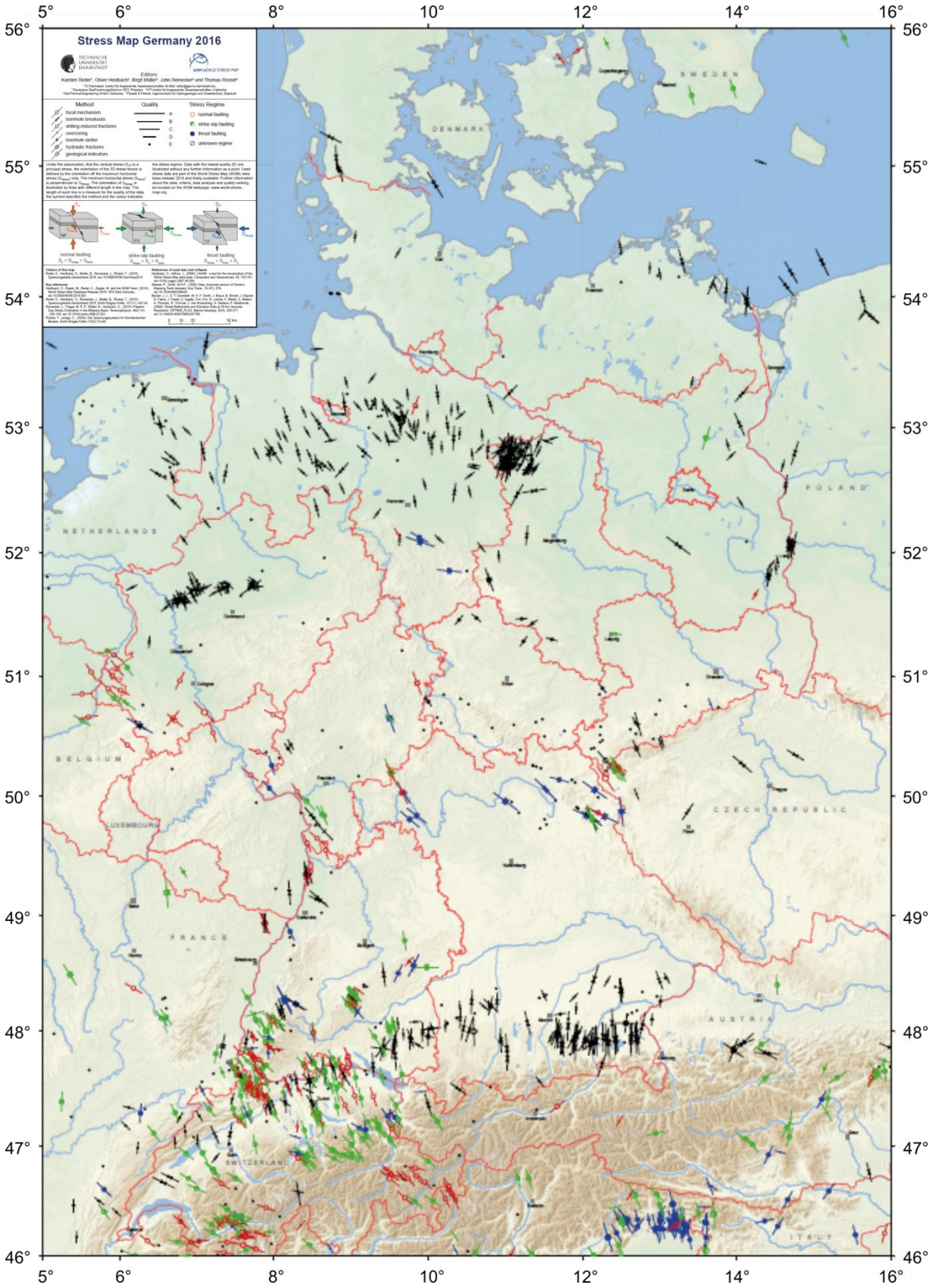

Fig. 2.4: Maximum principal stress orientation and stress regimes for Germany (modified after Reiter et al., 2016)

A general trend indicates relatively high stress ratios up to about 3 and at special locations even higher for $0.5 \cdot (SH + Sh)/SV$. With ongoing depth this ratio will becomes smaller and reach values close to 1 at great depths. This can be explained by thermo-mechanical theories incl. creep and failure criteria. Normally, the quasi-horizontal stresses are not equal, but show remarkable anisotropies. Often the ratio *SH*/*Sh* reaches values between 1 to 3, as documented exemplary by near-surface measurements in Hongkong (Fig. 2.5). Figure 6 shows the generalized average lateral earth pressure coefficient ($\lambda = 0.5 \cdot (SH + Sh)/SV$) for different regions around the world.

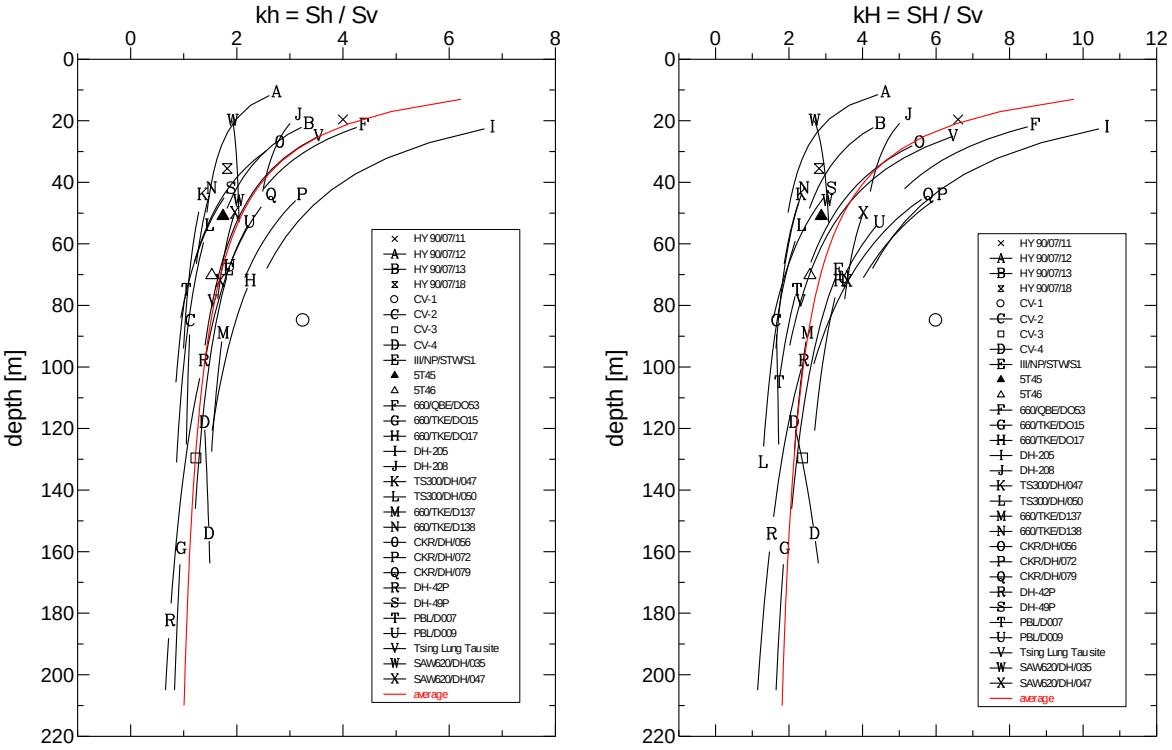

Fig. 2.5: Stress ratios k_h (left) and k_H (right) as function of depth determined in several boreholes in Hongkong

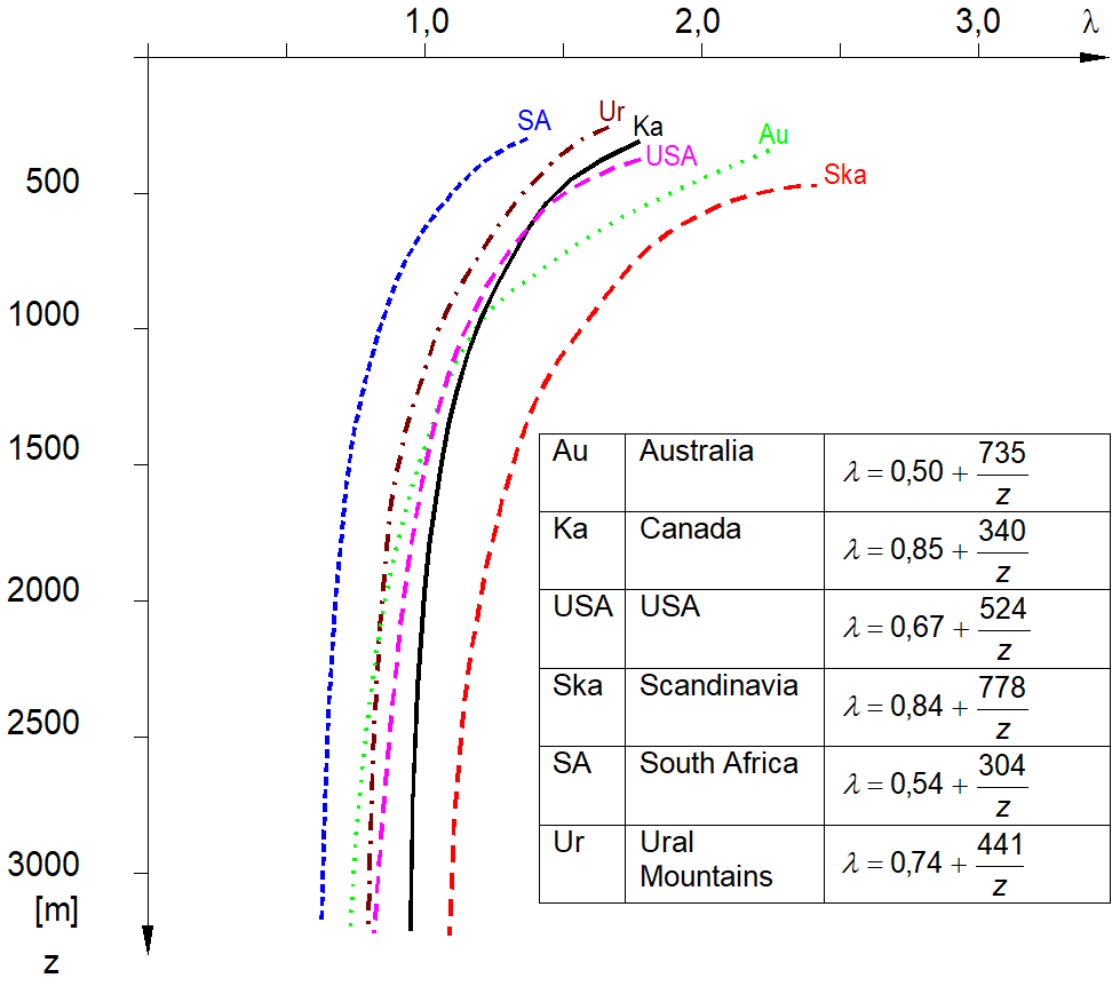

Au	Australia	$\lambda = 0{,}50 + \frac{735}{z}$
Ka	Canada	$\lambda = 0{,}85 + \frac{340}{z}$
USA	USA	$\lambda = 0{,}67 + \frac{524}{z}$
Ska	Scandinavia	$\lambda = 0{,}84 + \frac{778}{z}$
SA	South Africa	$\lambda = 0{,}54 + \frac{304}{z}$
Ur	Ural Mountains	$\lambda = 0{,}74 + \frac{441}{z}$

Fig. 2.6: Average lateral earth pressure coefficient for different regions around the world

3 Simple analytical models

The simplest analytical model to explain the in-situ stress field and often used in soil mechanics is based on an isotropic elastic half space with impeded lateral deformation. Using Hook's law this leads to the following expressions for the vertical and lateral principal stress components:

$$SV = \rho g h$$

$$SH = Sh = \left(\frac{\nu}{1-\nu}\right) SV$$

Where:

ν = Poisson's ratio ($0 \leq \nu \leq 0.5$)

h = depth

g = gravitational constant (9.18 m/s^2)

ρ = density

The above-mentioned simple model predicts that lateral stresses are always lower than vertical. This is in conflict with most of the measurement results in rock masses.

Therefore, other models were developed to explain high horizontal stresses at the surface. One of them is the so-called shell-model, which assumes, that the solid crust is lying on a fluid core. Due to the gravitational forces additional tangential compressive stresses are induced inside the crust even direct at the surface. This model leads to the following expressions for the virgin stress field

$$SV = \rho g h$$
$$SH = Sh = \left(\frac{\nu}{1-\nu}\right) SV + \sigma_{t0},$$

Where σ_{to} is an additional horizontal stress component depending on the parameter of the shell model.

Based on frictional joint strength data, Byerlee (1978) has deduced the following relation based on the Mohr-Coulomb law:

$$\tau = 0.85\sigma_N \quad \text{for} \quad 3\,\text{MPa} \le \sigma_N \le 200\,\text{MPa},$$
$$\tau = 0.6\sigma_N + 50 \quad \textit{for} \quad 200\,\text{MPa} \le \sigma_N \le 1700\,\text{MPa}.$$

Byerlee's law gives the maximum shear stress τ, which can be transmitted at a certain normal stress σ_N for critical orientation of joints in relation to principal stresses. Therefore, this relation gives upper bounds for transferrable stresses inside the crust at larger scale.

Anderson (1951) reformulated the Mohr-Coulomb law in terms of principal stresses and obtained three expressions for reverse faulting, normal faulting and strike-slip faulting (μ = friction coefficient):

$$\sigma_1 - \sigma_3 = \frac{2\left(c + \mu\rho g h\right)}{\sqrt{\mu^2 + 1} - \mu} \quad \text{for reverse faulting}$$

$$\sigma_1 - \sigma_3 = \frac{-2\left(c - \mu\rho g h\right)}{\sqrt{\mu^2 + 1} + \mu} \quad \text{for normal faulting}$$

$$\sigma_1 - \sigma_3 = \frac{2\left(c - \mu\rho g h\right)}{\sqrt{\mu^2 + 1}} \quad \text{for strike-slip faulting}$$

Figure 3.1 illustrates exemplary Anderson's expressions under the assumption, that the vertical stress component is the intermediate component at a certain depth and the two horizontal stresses are the minor and major components. As long as the stress state (red point) is inside the triangular areas, failure is prevented, but if the stress state reaches the boundary, faulting occurs. If pore or joint water pressure exists, water pressure has to be subtracted from the total stresses and the expressions have to be re-written in terms of effective stresses, possibly under consideration of Biot's coefficient (Tan & Konietzky, 2014).

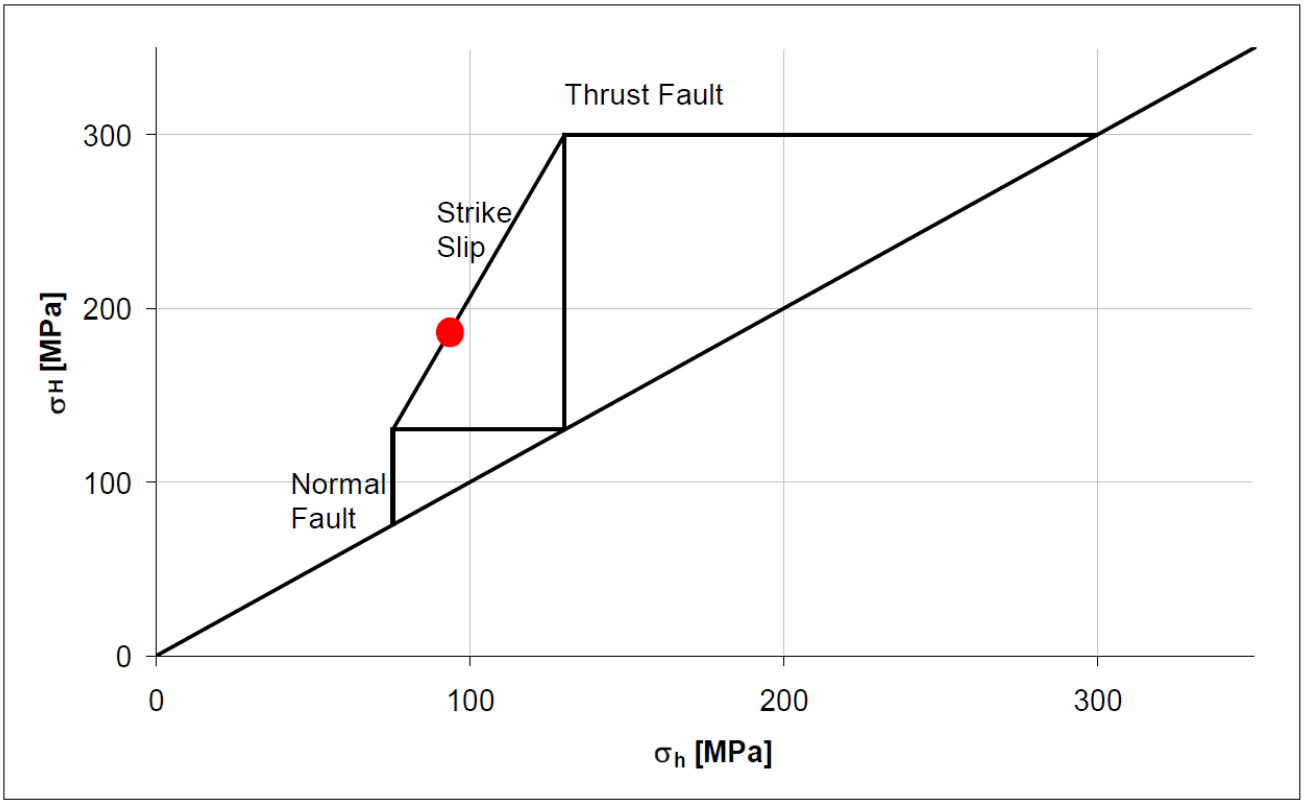

Fig. 3.1: Exemplary representation of Anderson's law with indication of stress regimes and certain stress state (red point), which indicates potential strike-slip failure

4 In-situ stress field measurements

Most reliable stress field measuring techniques, which can give both magnitudes and orientations of stresses, are hydraulic fracturing, borehole slotter, over-coring techniques, flat jacks and compensation methods on cores. Other techniques, like borehole breakout analysis, induced fracturing, fault plane solutions, moment tensor inversions, core splitting or geological features can act as indicators and provide only restricted, but very valuable information about the in-situ stress field. Some of the measurement techniques provide the complete stress tensor (absolute measurement), which means that both, stress magnitudes and orientations are provided either in absolute values (absolute measurements) or in terms of stress changes (differential measurements). Other techniques provide only orientations of the principal stresses, but no magnitudes – therefore, one can deduce the stress regime and others again provide only very limited information (Indicators). Table 1 gives an overview about stress measuring techniques currently in use.

One of the most popular methods is the hydro-frac stress measurement. This method allows the direct determination of the minimum principal stress component and their corresponding directions. Fig. 4.1 illustrates the tool, which consists of a straddle packer assembly, a coil tubing or drill pipe, a pump unit as well as pressure and flowrate sensors. According to fracture mechanical theory the hydraulic induced fracture propagates in the direction of the maximum principal stress and the measured shut-in pressure corresponds to the minimum principal stress component. Fig. 17 shows a typical recording of flow rate, packer pressure and interval pressure with breakdown and shut-in. Nowadays, often Televiewer (acoustic or optical tool) or Formation Micro Scanner (FMS, electrical tool) are used to detect fracture traces at the borehole wall (see also

Figures 18-22). Borehole breakouts (Fig. 24) are observed in the direction of the minimum principal stress component and can easily be determined by different techniques (Caliper Log, Televiewer). Another popular technique is overcoring, where a rock piece is overcored, deformation due to the destressing is recorded by strain gauges and evaluated in terms of equivalent in-situ stresses. More detailed description about this topic including measurement techniques is given by Zang & Stephansson (2010). The following photos and sketches illustrate some of the stress measurement methods listed in Table 1.

Table 1: Overview about stress measurement techniques

Method	Type of measurement	Examples / Measuring Techniques	Typical depth range of application
Relief methods	Absolute	Overcoring (Fig. 4.1-4.5) Borehole slotter (Fig. 4.11) Diametrical core deformation (Fig. 4.25)	up to several 10 or 100 m
Compensation method in-situ	Absolute	Pressure cell (Fig. 4.12) Flatjack (Fig. 4.13)	up to several 10 m
Compensation method at cores	Absolute	Wave velocity anisotropy Seismoacoustic emission RACOS (Fig. 4.14)	Up to several 1000 m
Core analysis	Indicator	Core splitting, discing (Fig. 4.15)	Up to several 1000 m
Hydraulic fracturing and induced hydraulic fractures	Absolute	Hydraulic fracturing (Fig. 4.16-4.17) Pneumatic fracturing Drilling mud induced fracturing	Up to several 1000 m
Seismic methods	Stress regime	Moment tensor inversion Fault plane solutions of earthquakes and induced seismic events	Up to several 1000 m
Borehole breakouts	Stress regime	Televiewer (Fig 4.18-4.20) FMS (Fig. Fig. 4.21-4.23) Caliper-Log (Fig. 4.24)	Up to several 1000 m
Paleomagnetik	Indicator	Magnetic field measurements	Up to several 1000 m
Strain field method, Analysis of tectonic elements	Stress regime	Fault or fracture analysis	Up to several 100 or 1000 m
Stiff inclusion method	Differential	Hydraulic pressure cell	up to several 10 m
LVDT cell	Absolute	Overcoring with LVDT cell (Fig. 4.6-4.9)	up to several meters

Convergence measurement	Absolute	Overcoring with convergence measurement (Fig. 4.10)	Up to several 100 m

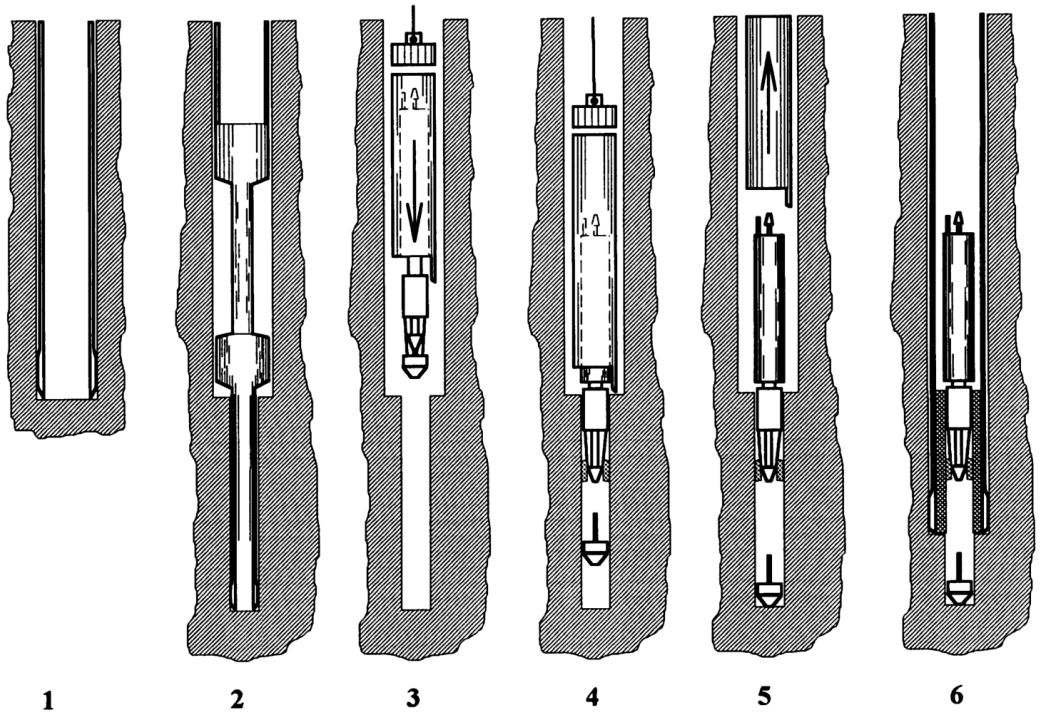

Fig 4.1: Principle of over-coring technology: (1) drilling of main borehole (2) pilot borehole and recover core for appraisal (3) lower probe (4) probe released and gauges bonded to pilot hole (5) raise installation tool, probe bonded (6) over-coring probe (company material)

Fig. 4.2: CSIRO-HI-Cell based on over-coring technology (company material)

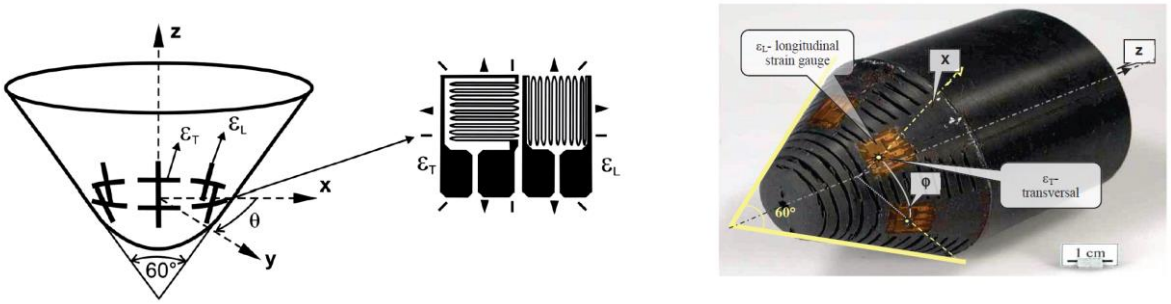

Fig. 4.3: CCBO-Cell based on over-coring technology (Waclawik et al., 2016)

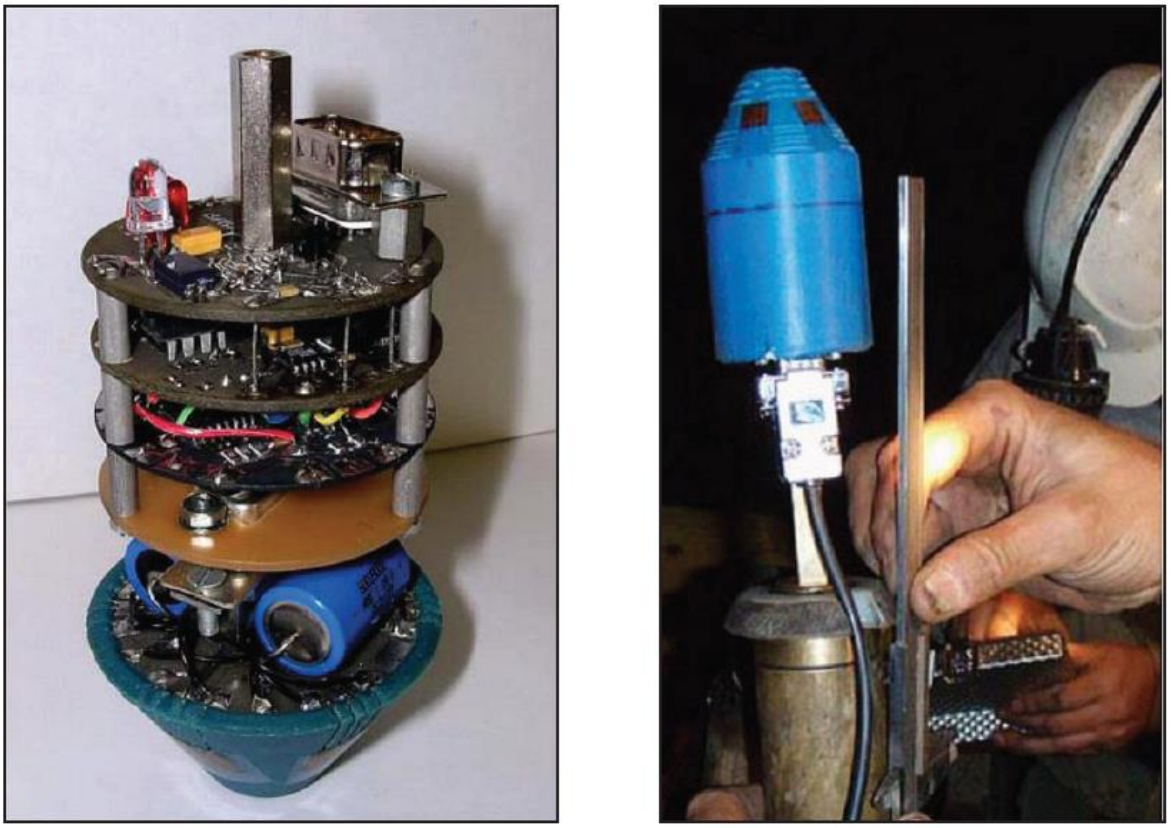

Fig. 4.4: CCBO-Cell (Waclawik et al., 2016)

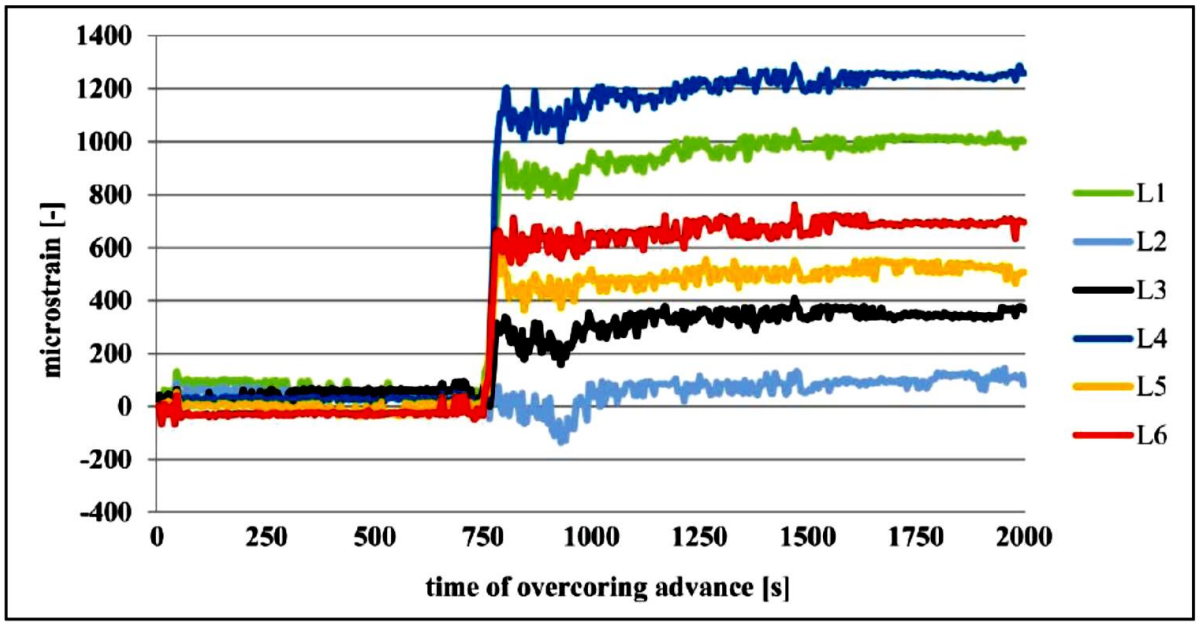

Fig. 4.5: Example of CCBO-Cell overcoring strain response in a sandstone (Waclawik et al., 2016)

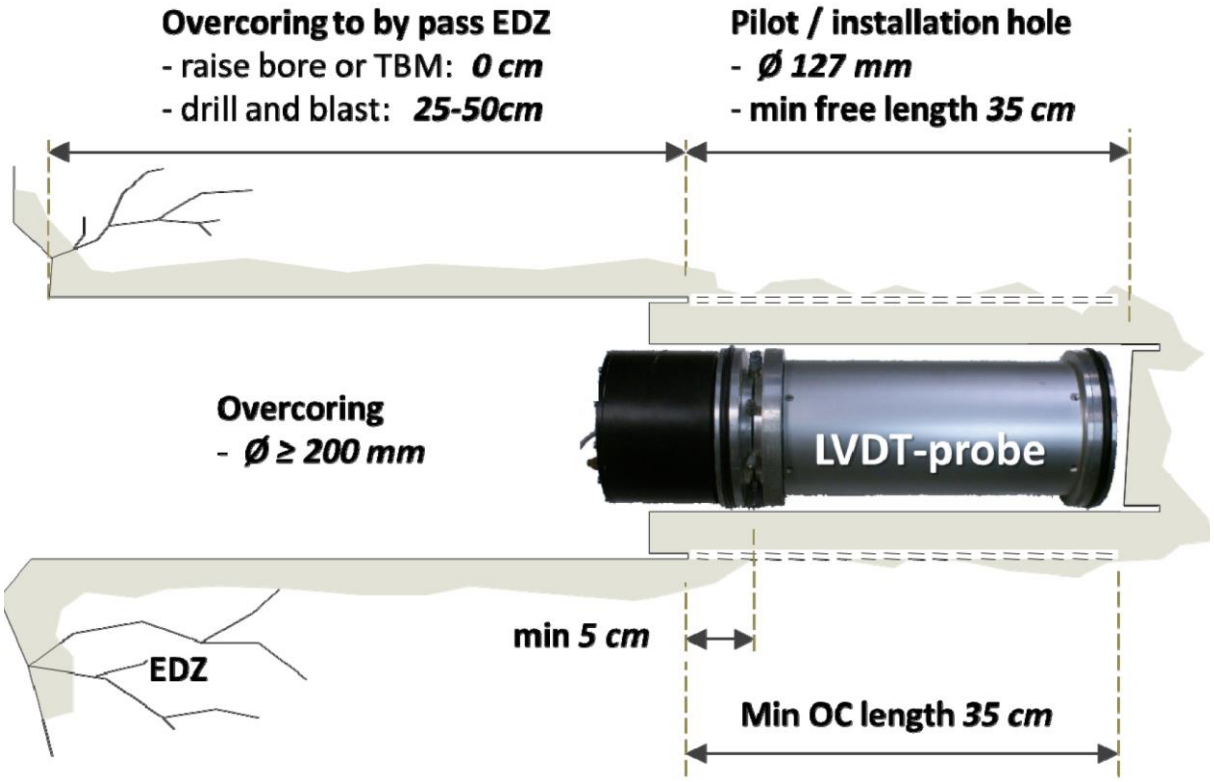

Fig. 4.6: Installation of a LVDT cell inside a borehole (Hakala et al. 2013).

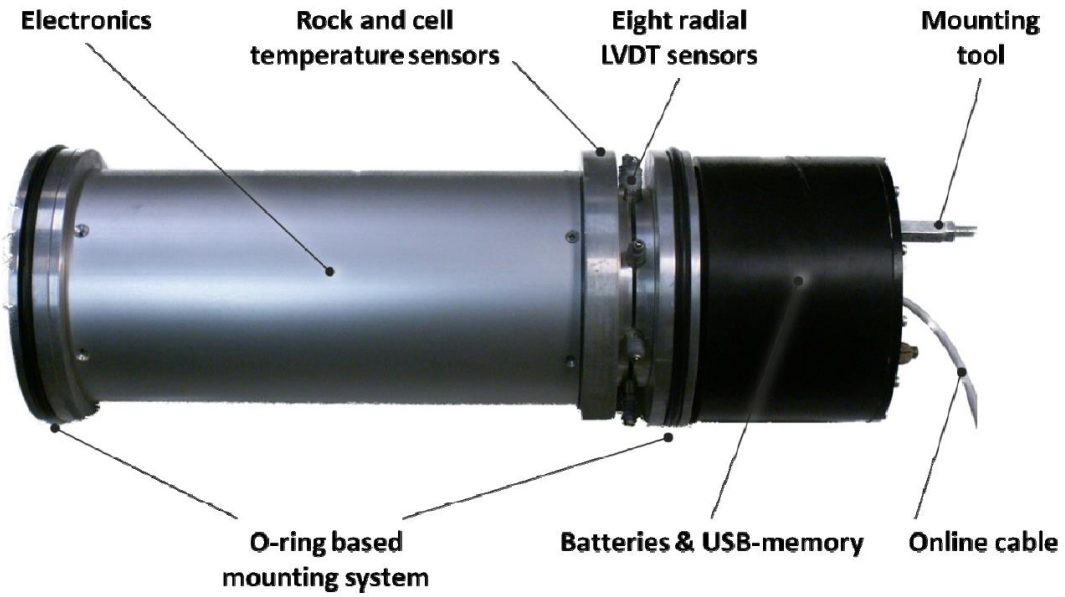

Fig. 4.7: Main components of LVDT cell (Hakala et al. 2013).

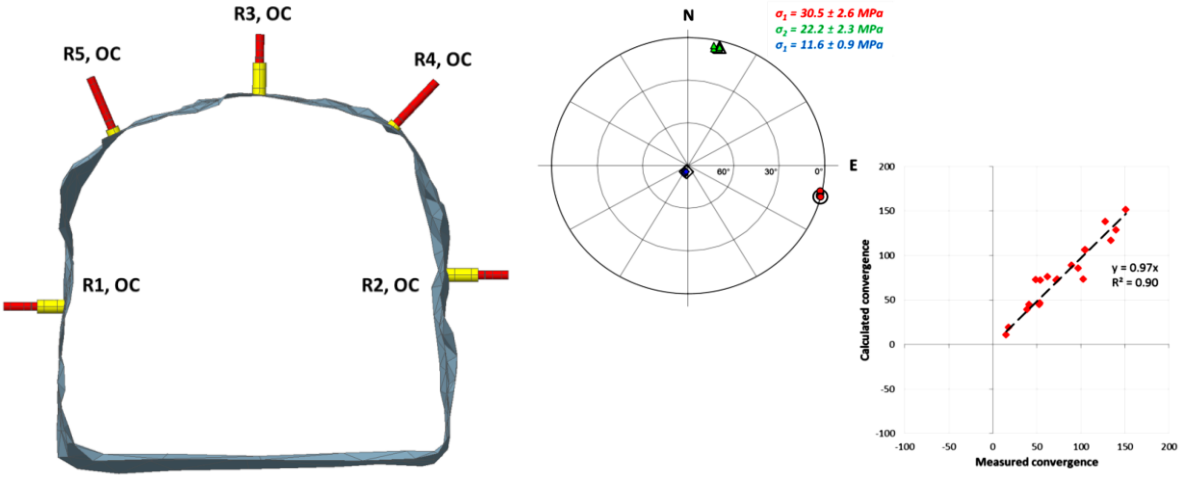

Fig. 4.8: Right: Typical layout of LVDT cell measurement, Left: typical measurement result (Hakala et al. 2013).

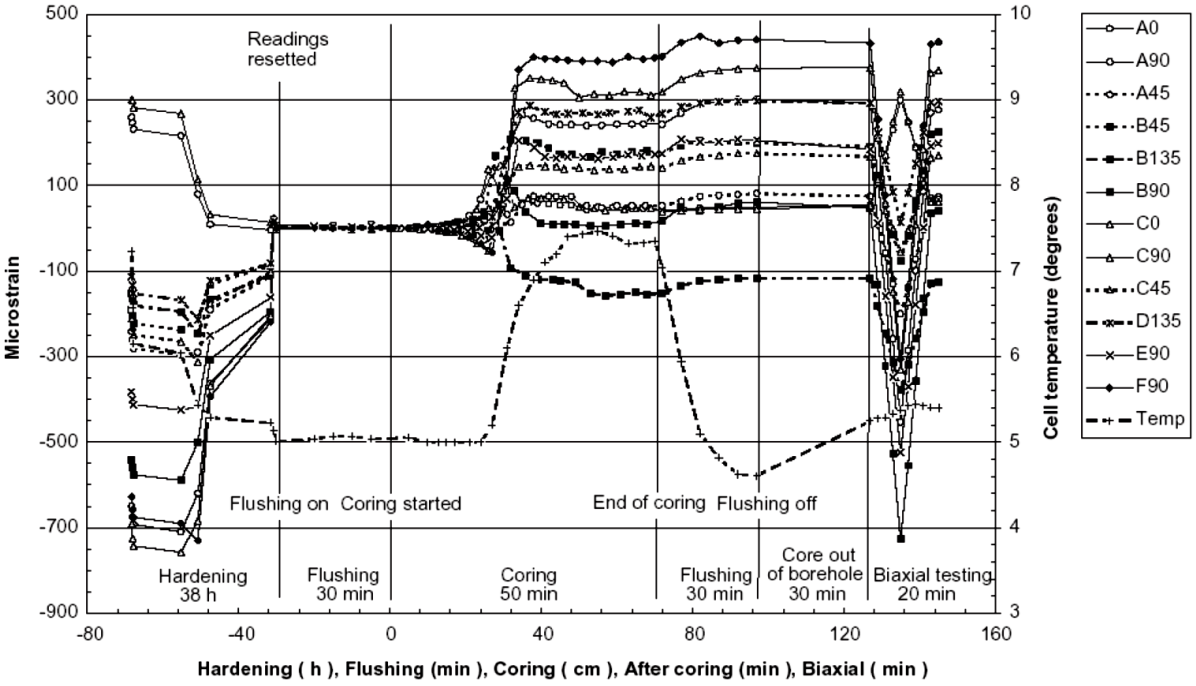

Fig. 4.9: Example of measured strains before, during, and after over-coring (Hakala et al., 2003)

Fig. 4.10: Overcoring probe measuring 4 diametric convergences with 8 sensors (company material)

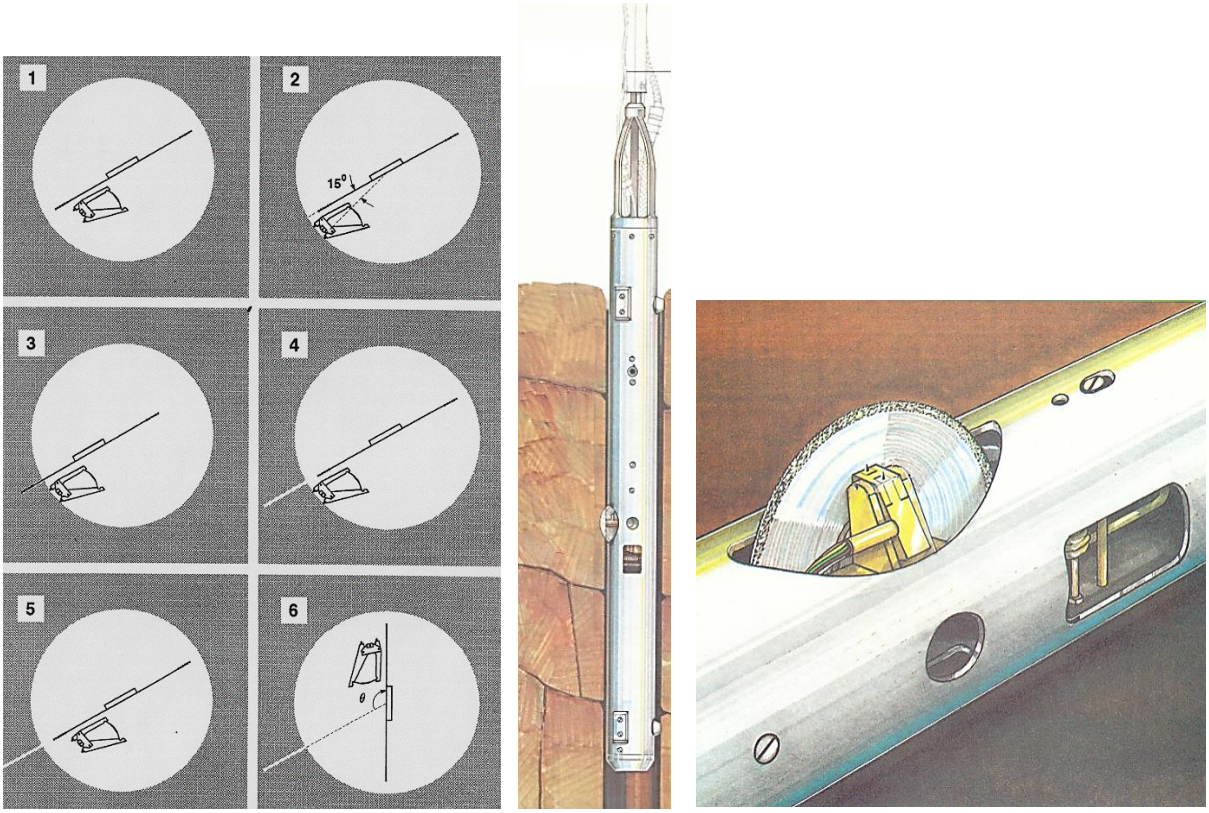

Fig. 4.11: Principal of borehole slotter (company material)

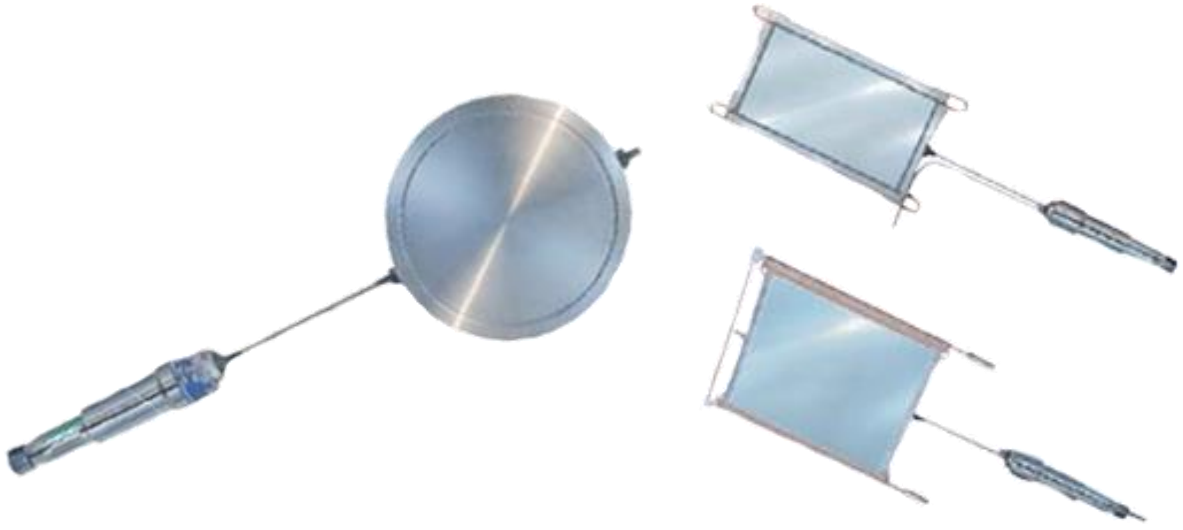

Fig. 4.12: Typical pressure cells (company material)

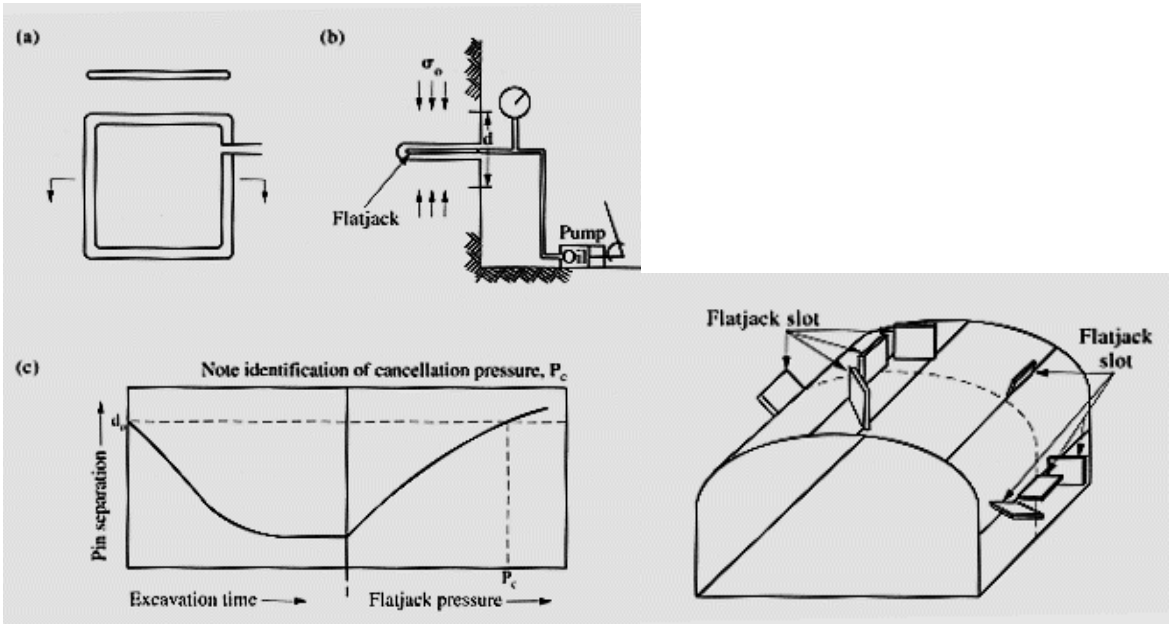

Fig. 4.13: Principal of pressure cells (flatjack)

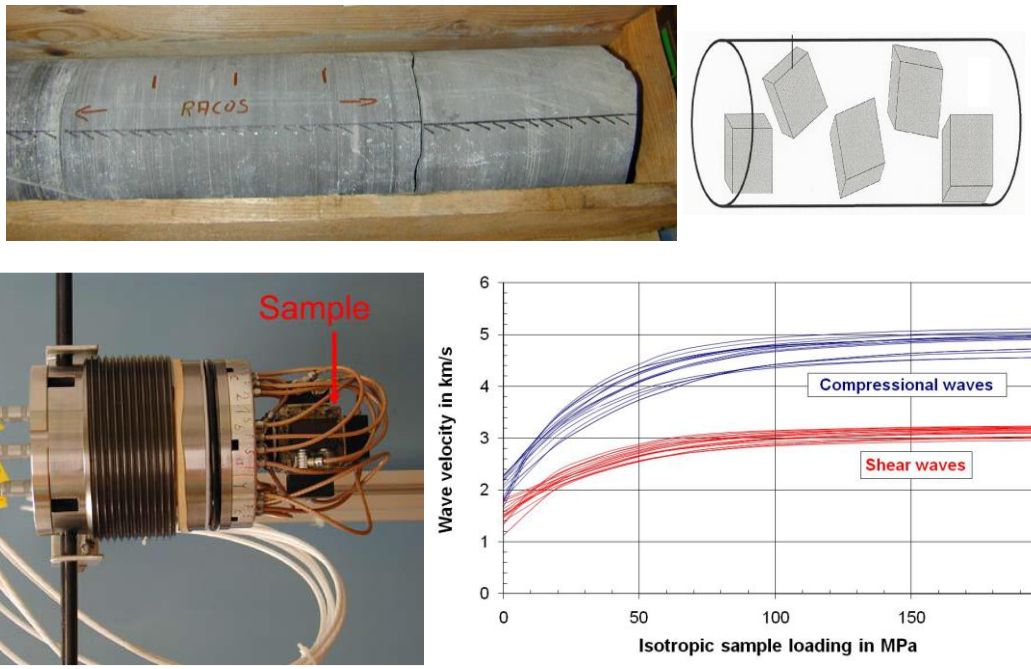

Fig. 4.14: Main steps of core compensation method: Sample preparation, reloading of samples and monitoring of the seismic wave velocities (Braun 2014)

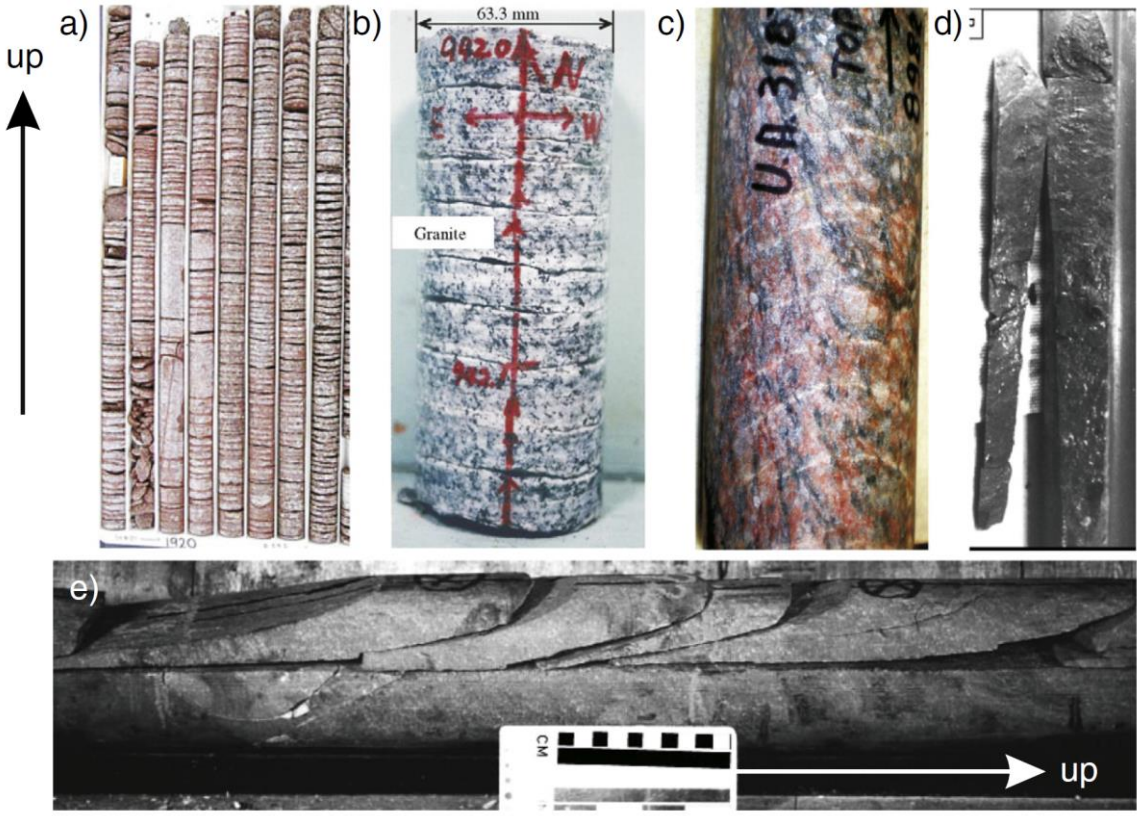

Fig. 4.15: Typical core splitting / discing behaviour (Schmitt et al. 2012)

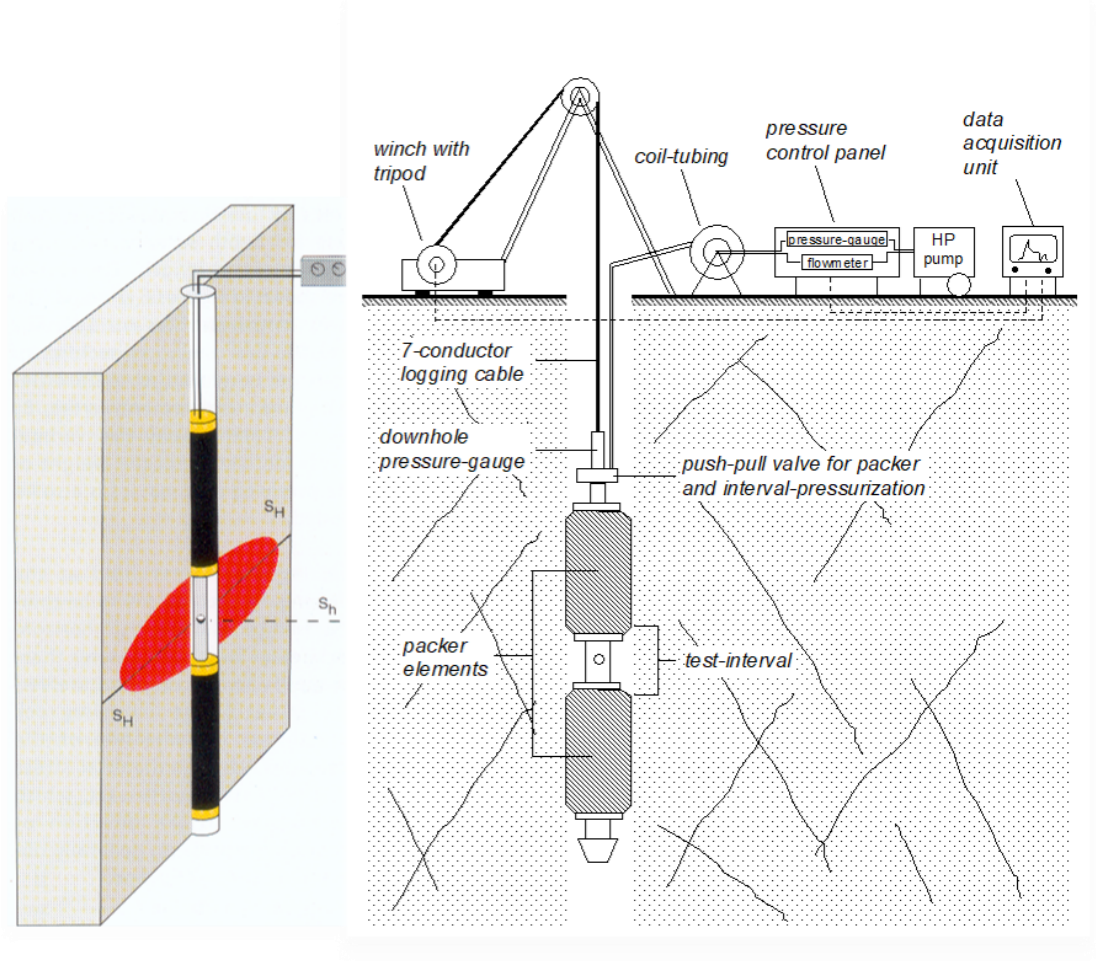

Fig. 4.16: Hydrofrac-equipment and fracture propagation according to stress field

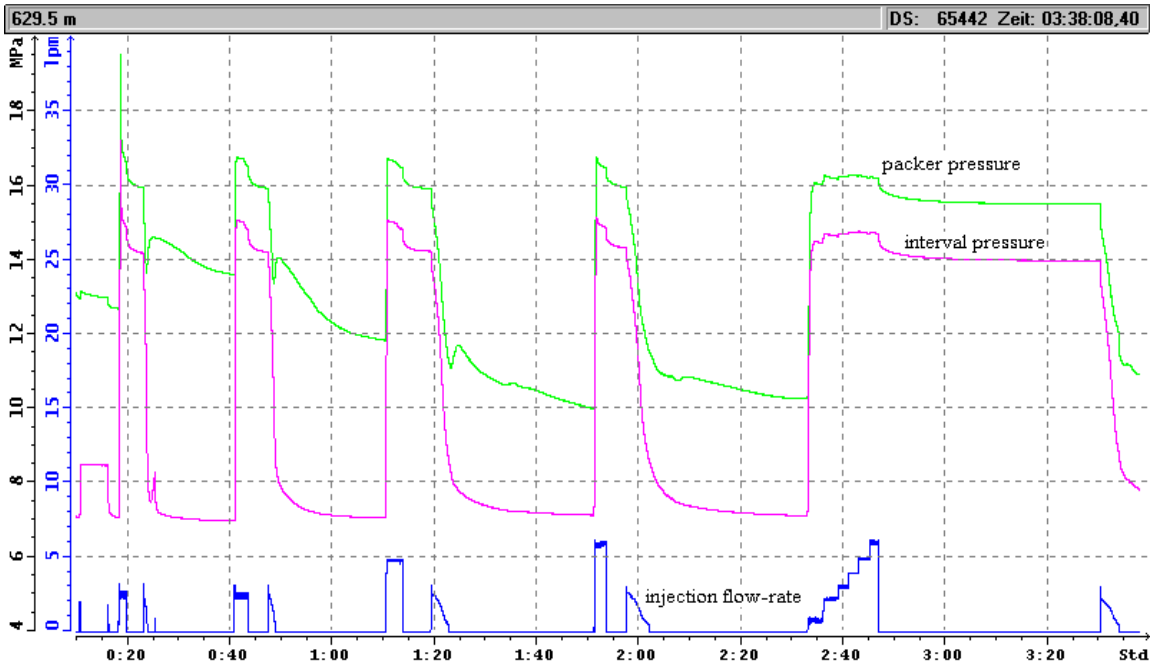

Fig. 4.17: Typical hydrofrac recording (packer pressure, interval pressure and pump-rate)

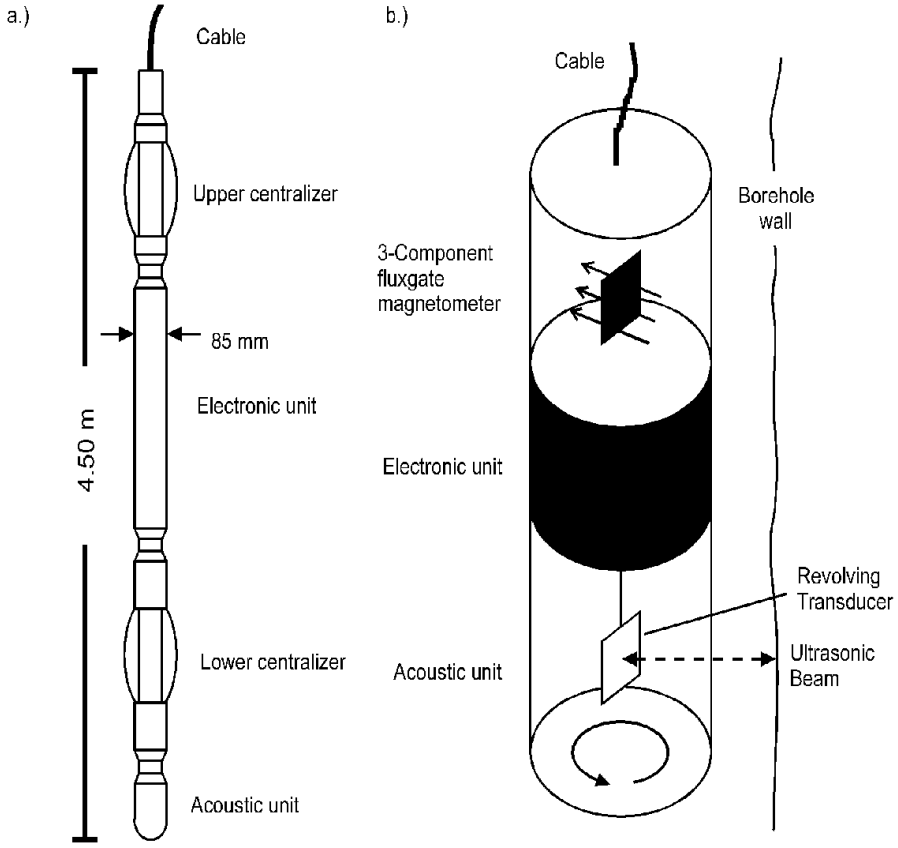

Fig. 4.18: Principal sketch of borehole acoustic televiewer

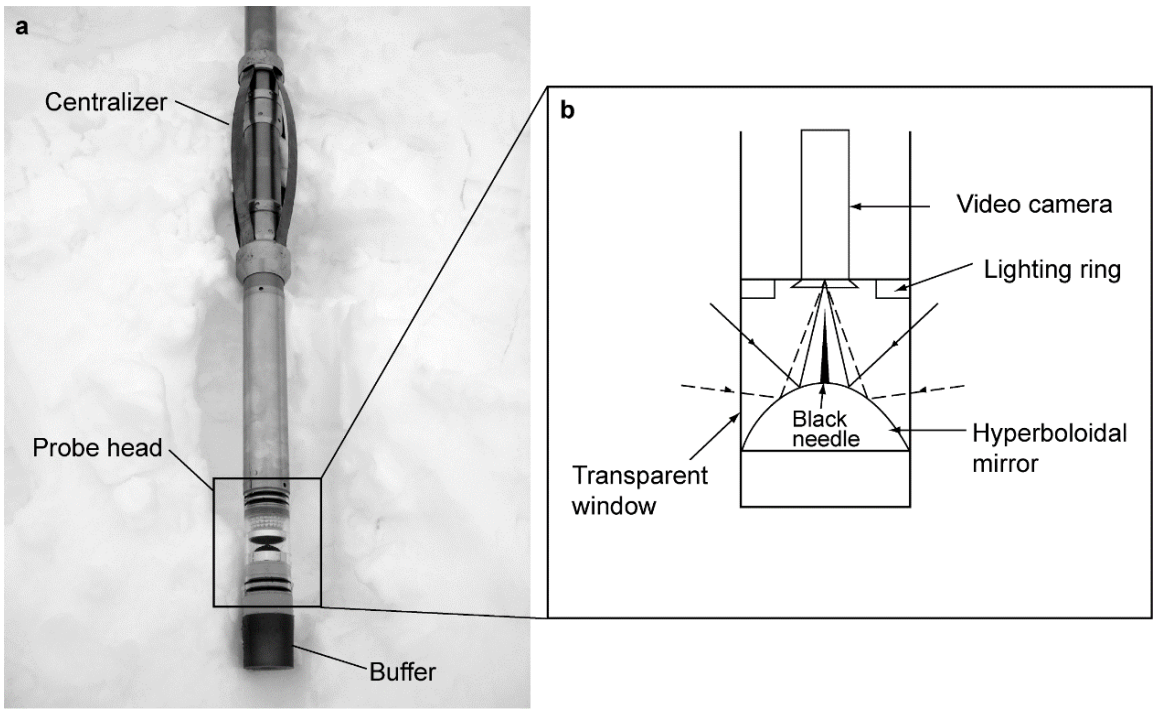

Fig. 4.19: Typical optical Televiewer (company material)

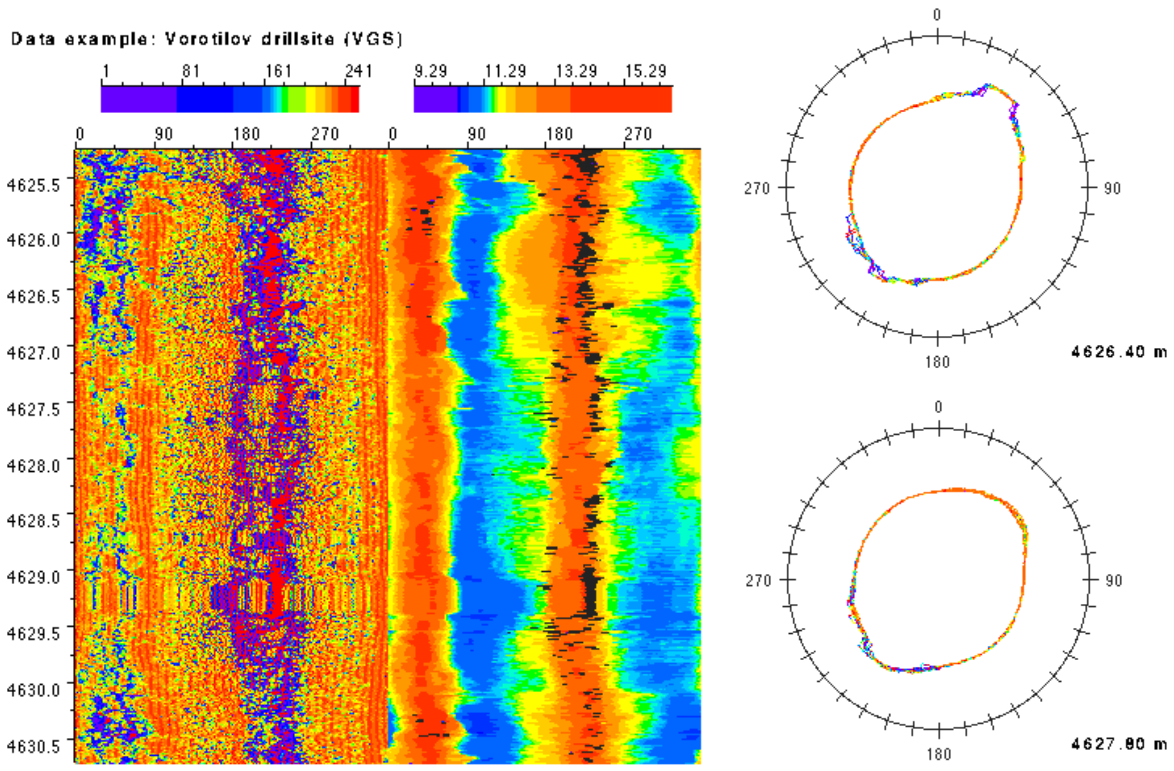

Fig. 4.20: Borehole breakout detection based on acoustic Televiewer data

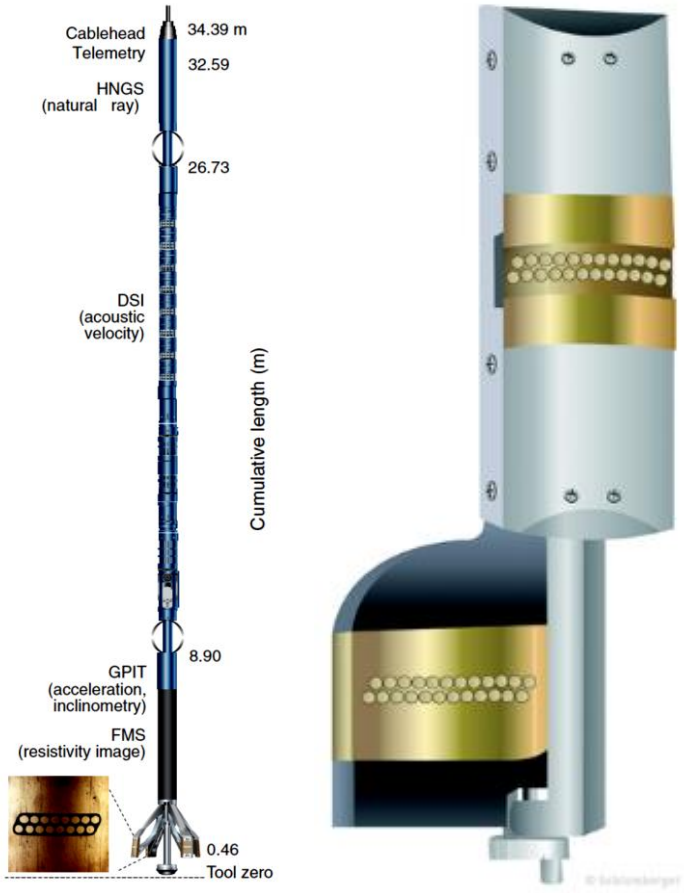

Fig. 4.21: Typical Formation Micro Scanner (FMS) with detailed view of sensor pads (company material)

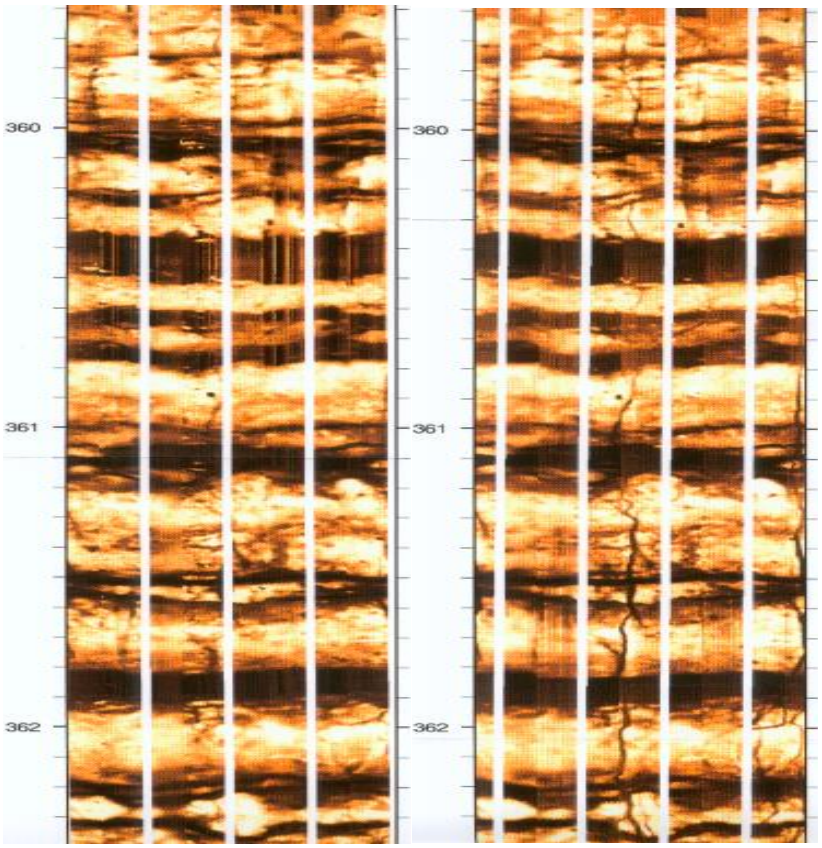

Fig. 4.22: Typical FMS recording before (left) and after (right) hydrofrac operation with clear indication of two vertical cracks at about 180° and 360°

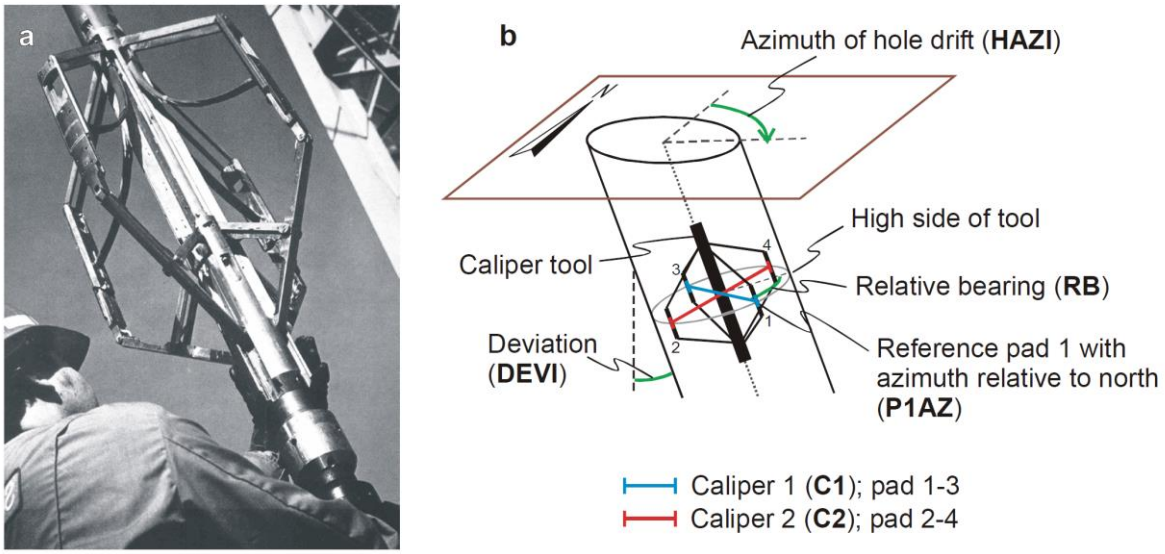

Fig. 4.23: Four-Arm-Caliper-Tool, used for breakout analysis by rotation and simultaneous vertical movement inside the borehole (Reinecker et al. 2003)

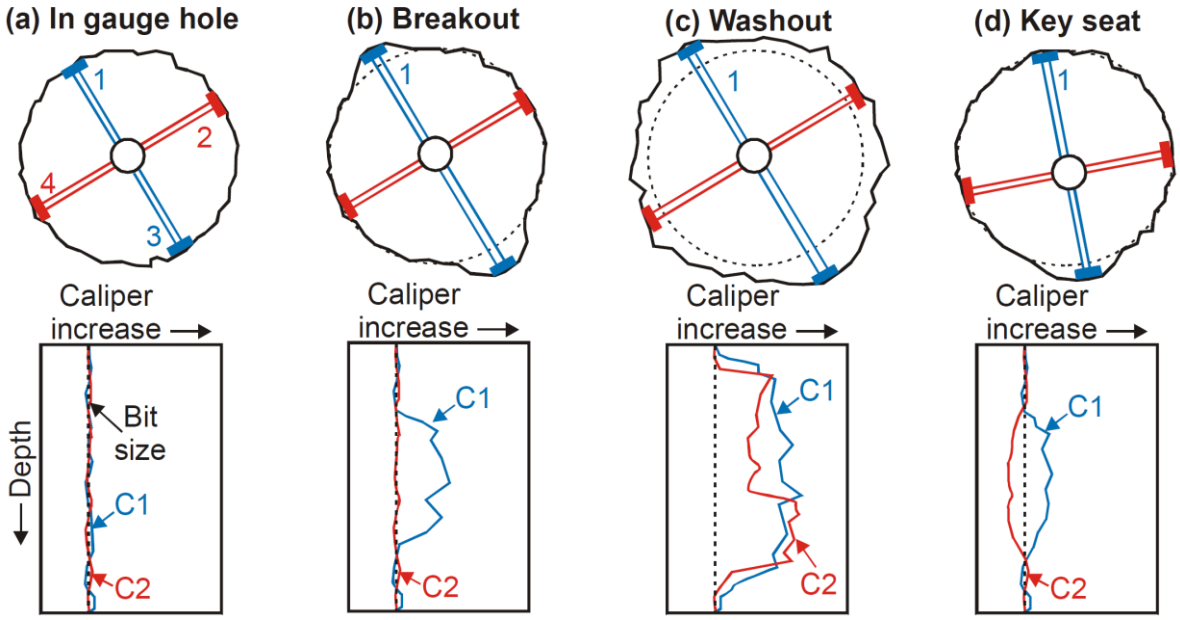

Fig. 4.24: Typical borehole shapes detected by caliper measurements (Reinicke et al. 2003)

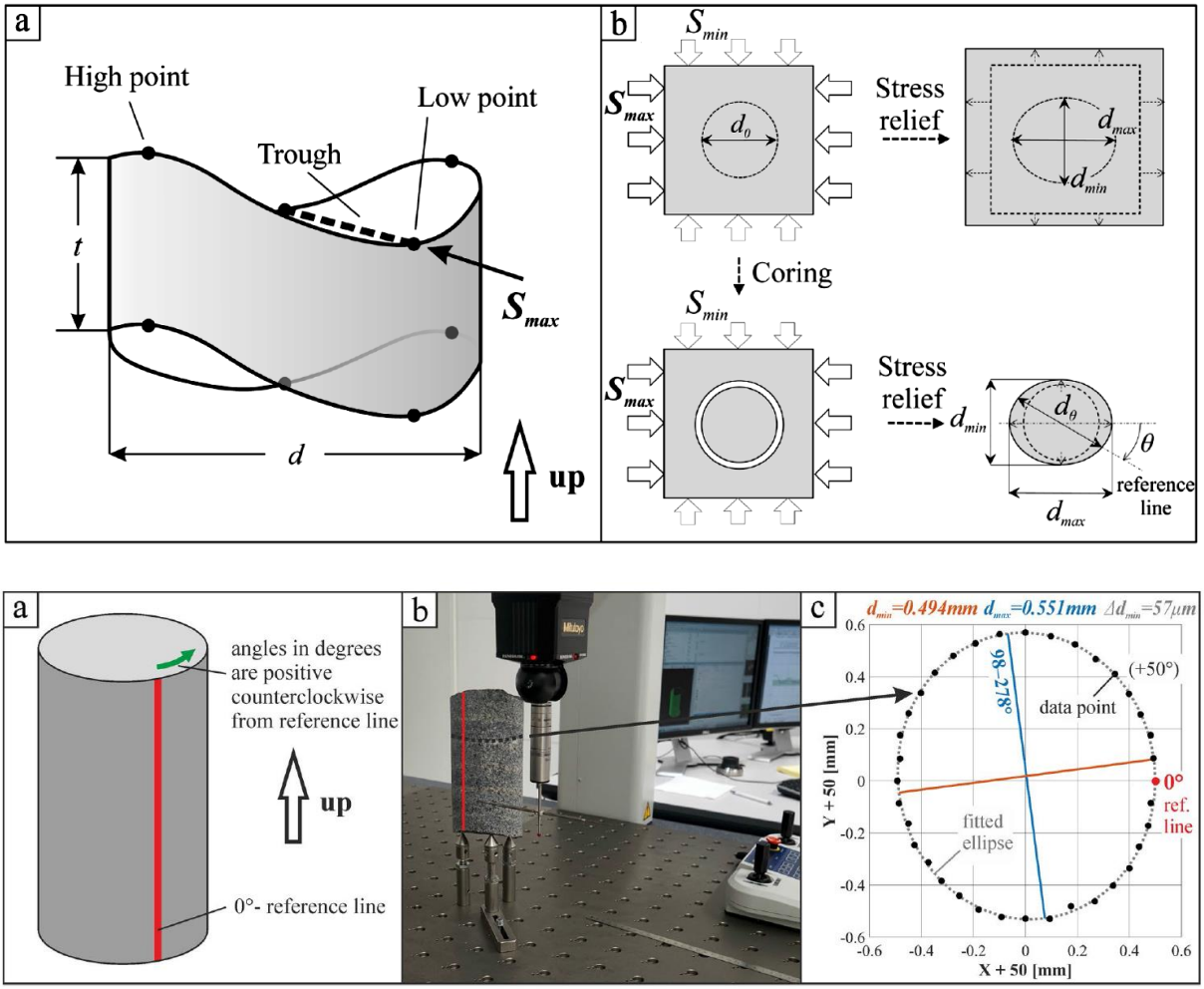

Fig. 4.25: Diametrical core deformation analysis: above: principle of the measurement method, below: measurement example (Ziegler & Valley 2021).

5 Calibrated numerical stress field modelling

The mechanical as well as the HTM-coupled behaviour of rock masses is mainly governed by the material characteristics and the stress field. In general, a lot of effort is spent into the determination of material parameters and the choice or development of corresponding constitutive laws to describe the rock mass behaviour. Unfortunately, often less effort is spent for the determination of the in-situ stress field, although it has a decisive impact on the general system behaviour. This is mainly because stress measurements are expensive, complicated to conduct and results are difficult to interpret.

To get a more reliable and comprehensive knowledge about the stress field, stress measurements were combined with numerical stress field modelling (e.g. Konietzky 2005). There are several reasons, why in-situ stress field measurements should be combined with stress field modelling:

- In-situ stress field measurements are always very local ‘point measurements’ and do not allow deducing complete stress fields for bigger 3D volumes.
- Evaluation of stress measurements include often several assumptions (e.g. that the vertical is a principal stress axis or material behaviour is isotropic elastic), which has to be confirmed, rejected or corrected.
- Stress field modelling in conjunction with measurements allows the separation of different stress field components, e.g. tectonic, gravitational, local, regional, thermal ones.
- Stress field modelling allows the determination of complete stress profiles, the determination of stresses outside of the investigated area and the reduction of uncertainty and variation in measurement data.

The combination of stress measurements and numerical simulations, also called “calibrated numerical stress field modelling”, was developed in parallel in applied geology, civil engineering (especially in tunnelling) and mining and underground radioactive waste storage (e.g. Konietzky & Blümling 1995, Konietzky & Rummel 2004, Konietzky 2005, Zang & Stephansson 2010).

A conceptual stress field model has to consider the following aspects:

- Choice of suited numerical simulation technique and code
- Incorporation of geological layering and formations (stratigraphy)
- Discontinuities, like faults, fractures, bedding planes, interfaces etc.
- Choice of appropriate constitutive laws and parameters for describing the geological units and discontinuities (e.g. elasto-plastic, visco-elasto-plastic)
- Groundwater (pore and joint water pressure)
- Topography
- Incorporation of geological history, especially erosion (e.g. overconsolidation effect)
- Choice of appropriate boundary conditions, especially tectonic stresses
- Available measurement results and indicators for calibration
- Determination of appropriate model dimensions and meshing

Due to reasons mentioned already in chapter 1 the stress fields in rock masses are often quite complex, that means orientation and magnitudes of stresses can change within relatively short distances. Exemplary, Figs. 5.1 to 5.5 show combined results of hydrofrac stress measurements and numerical stress field simulations. This case study shows, that in-situ stress can change quite dramatically over short distances due to influence of topography, faulting and overconsolidation.

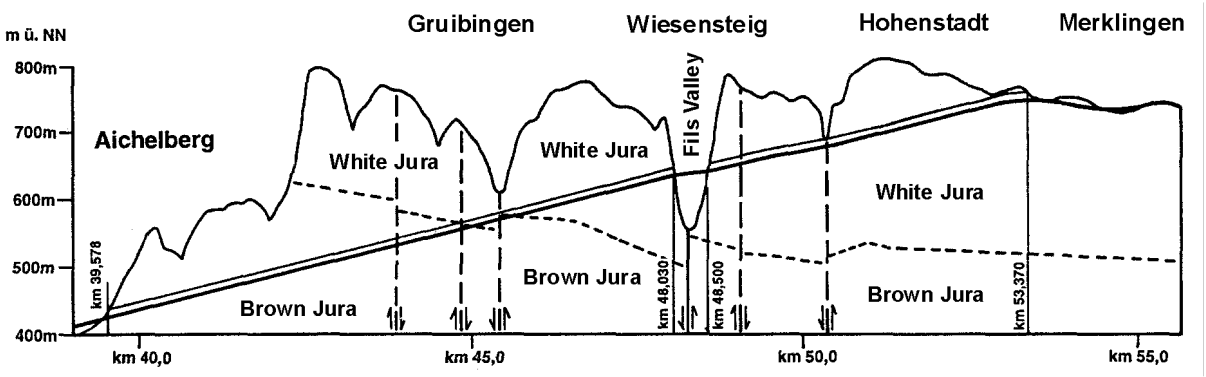

Fig. 5.1: Vertical cross section through rock mass with tunnel route and main geological features (Konietzky et al. 2001)

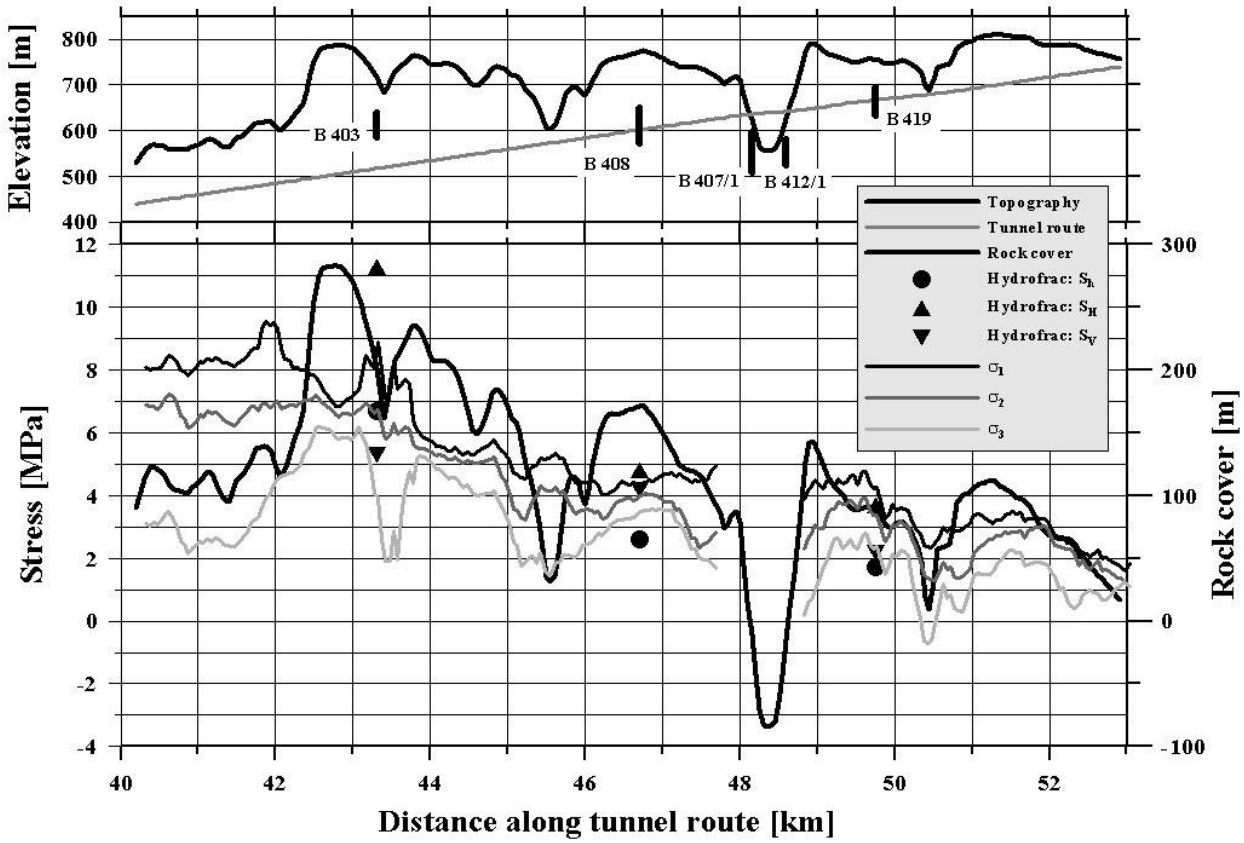

Fig. 5.2: Topography, tunnel route and hydrofrac measurement sections (top); measured and simulated profiles of principal stress components along tunnel axis together with topography (bottom), (Konietzky et al. 2001)

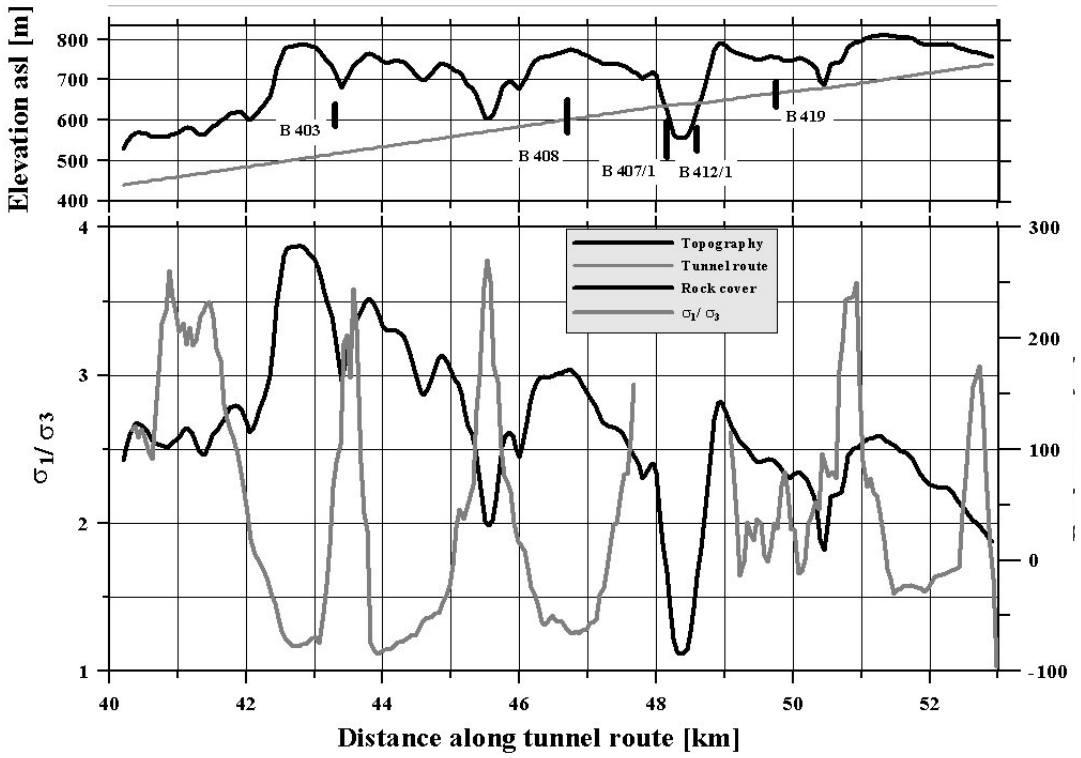

Fig. 5.3: Topography, tunnel route and hydrofrac measurement sections (top), measured and simulated stress ratio along tunnel axis together with topography (bottom), (Konietzky et al. 2001)

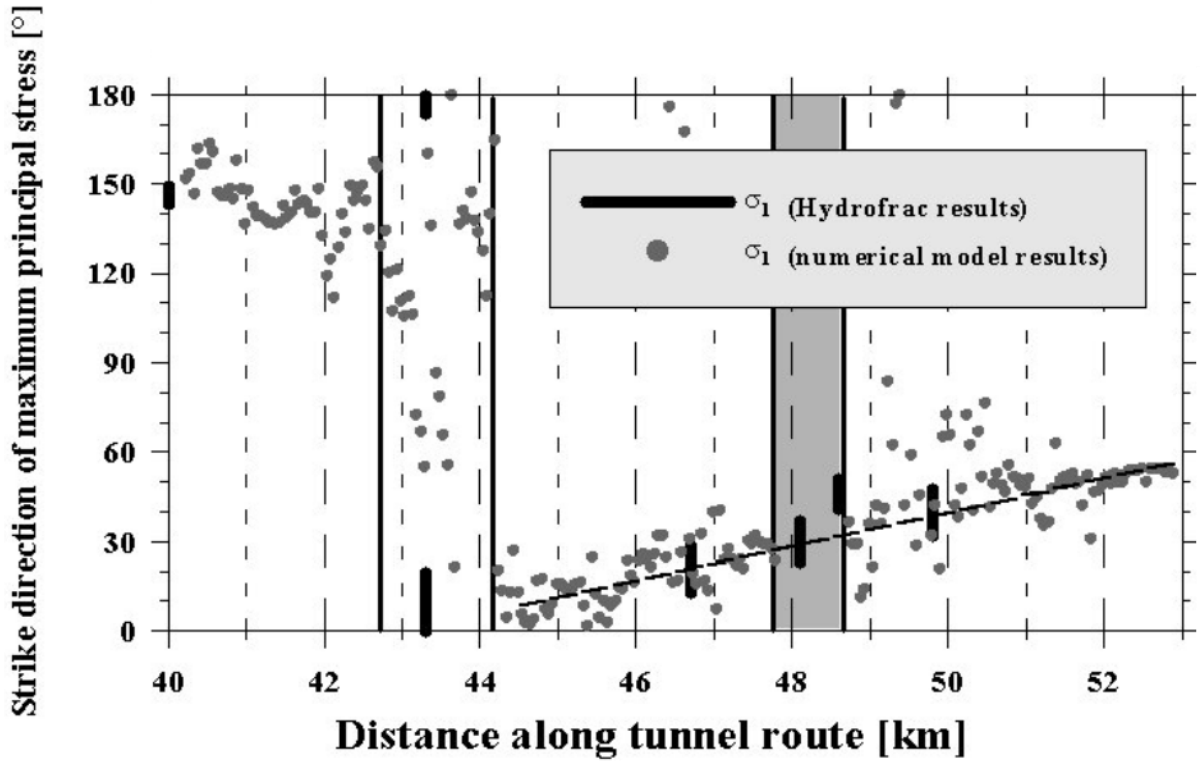

Fig. 5.4: Measured and simulated strike direction or maximum quasi-horizontal stress component along tunnel axis (Konietzky et al. 2001)

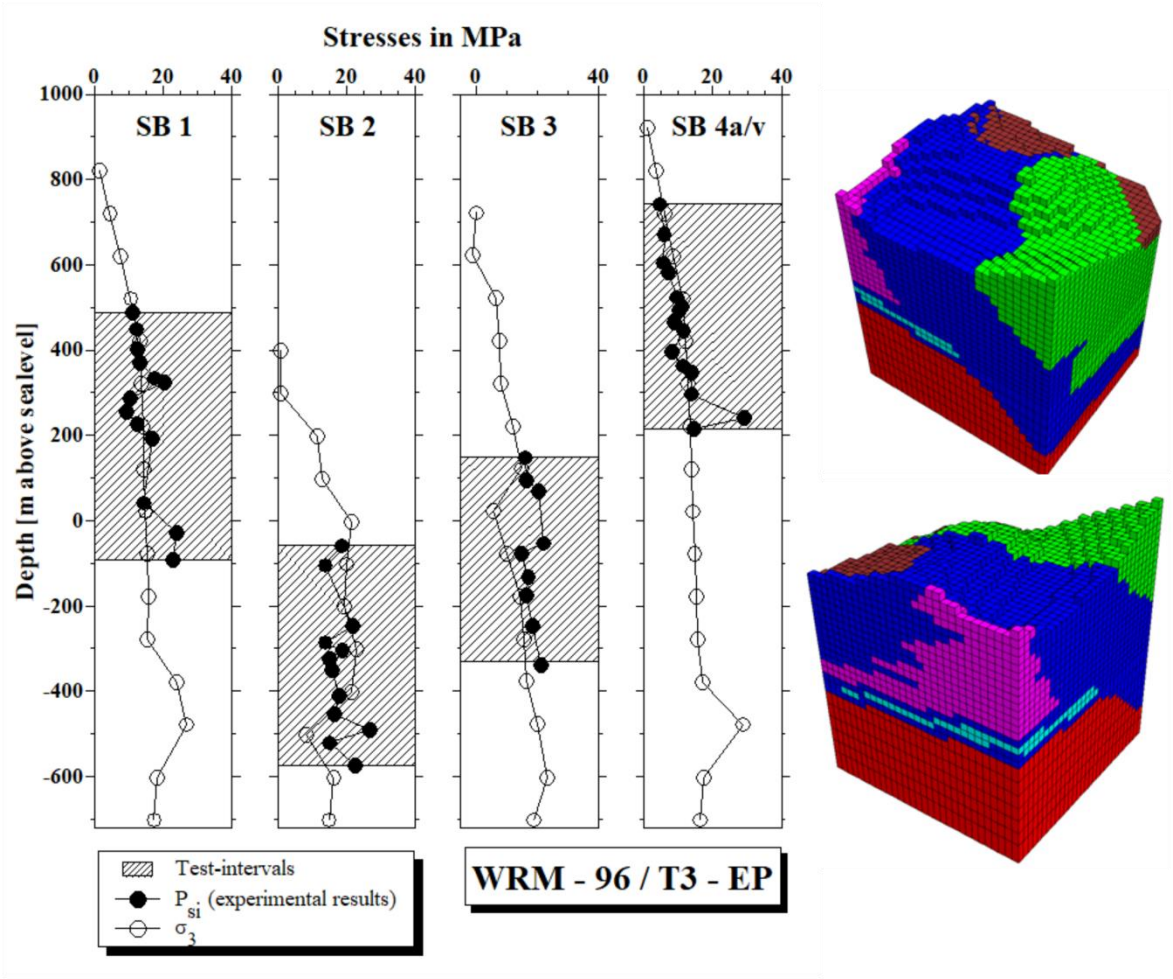

Fig. 5.5: Measured (filled circles) and simulated (open circles) stress profiles for minimum principal stress component along 4 boreholes and inner part of corresponding numerical model, where different colors correspond to different geological units with different properties (Wellenberg, Switzerland; Konietzky (1995))

6 ISRM suggested methods

The International Society for Rock Mechanics (ISRM) has issued a few suggestions how to perform in-situ stress measurements (ISRM Suggested Methods). These documents describe the general methodology and the different methods. They give also hints how to evaluate the measuring data and to transfer them into a reliable model for the specific site. In total five such documents exist so far (see chapter 7). A general overview is given by Ljunggren et al. (2003).

7 World Stress Map (WSM)

WSM is an open project managed by the German Research Centre for Geosciences (Potsdam, Germany) and contains already more than 40,000 data sets. The data sets contain stress data in terms of orientation and magnitudes obtained by different stress measurement methods. The data are categorised according to their quality (see Fig. 7.1 and 7.2). It should be noticed, that for all WSM data it is assumed, that the vertical direction is a principal stress direction and consequently two horizontal principal stress direction exist (S_{Hmax} and S_{hmin}). Please note also, that this assumption might be wrong, especially if we consider near-surface layers, where other effects like topography become important.

Fig. 7.3 illustrates how a complete 3D stress field can be deduced by numerical stress field modelling using point data from the WSM as start point but considering also the geology. Fig. 7.3 documents also, that the even virgin stress fields can be quite inhomogeneous and anisotropic.

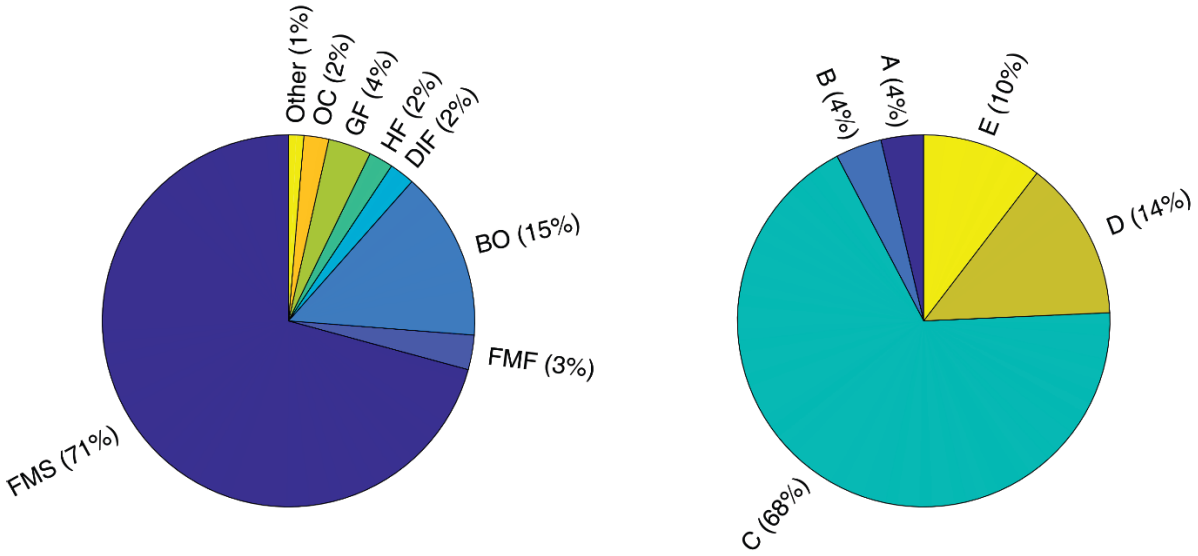

Fig. 7.1: WSM statistics (stress orientation), left chart: stress measurement methods (FMS: focal mechanism, FMF: formal inversion of focal mechanism, DIF: drilling induced tensile fractures, HF: hydraulic fracturing, GF: geological indicators, OC: over-coring; right chart: distribution of data quality (declining quality from A to E) (Ziegler et al., 2020)

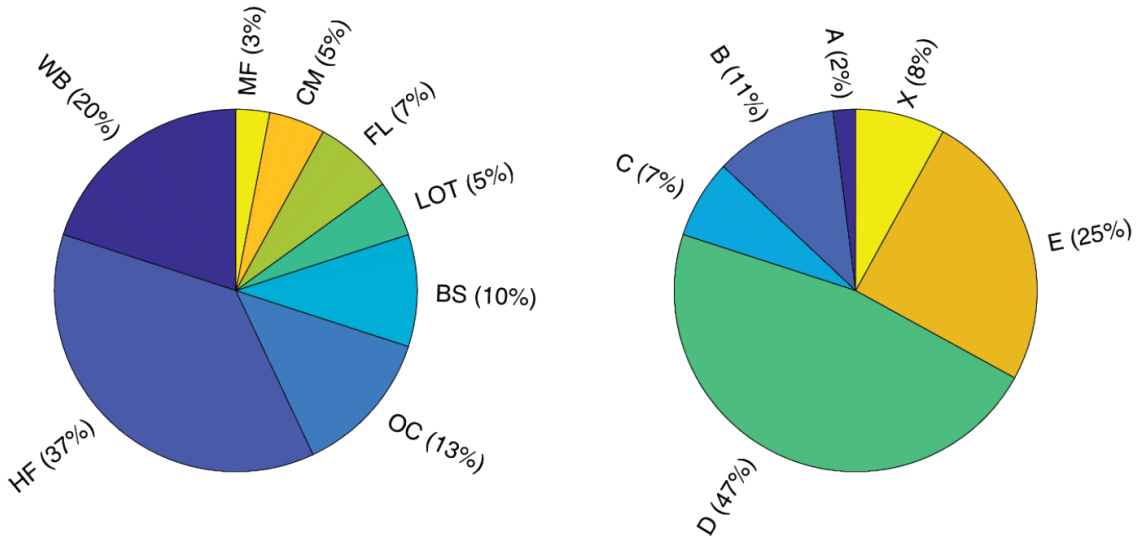

Fig. 7.2: WSM statistics (stress magnitude), left chart: stress measurement methods (WB: wellbore fluid measurements, HF: hydraulic fracturing, OC: over-coring, BS: borehole slotter, LOT: leak off and formation integrity test, FL: frictional limit consideration, CM: core measurements, MF: mini fracs; right chart: distribution of data quality (declining quality from A to E) (Ziegler et al., 2020)

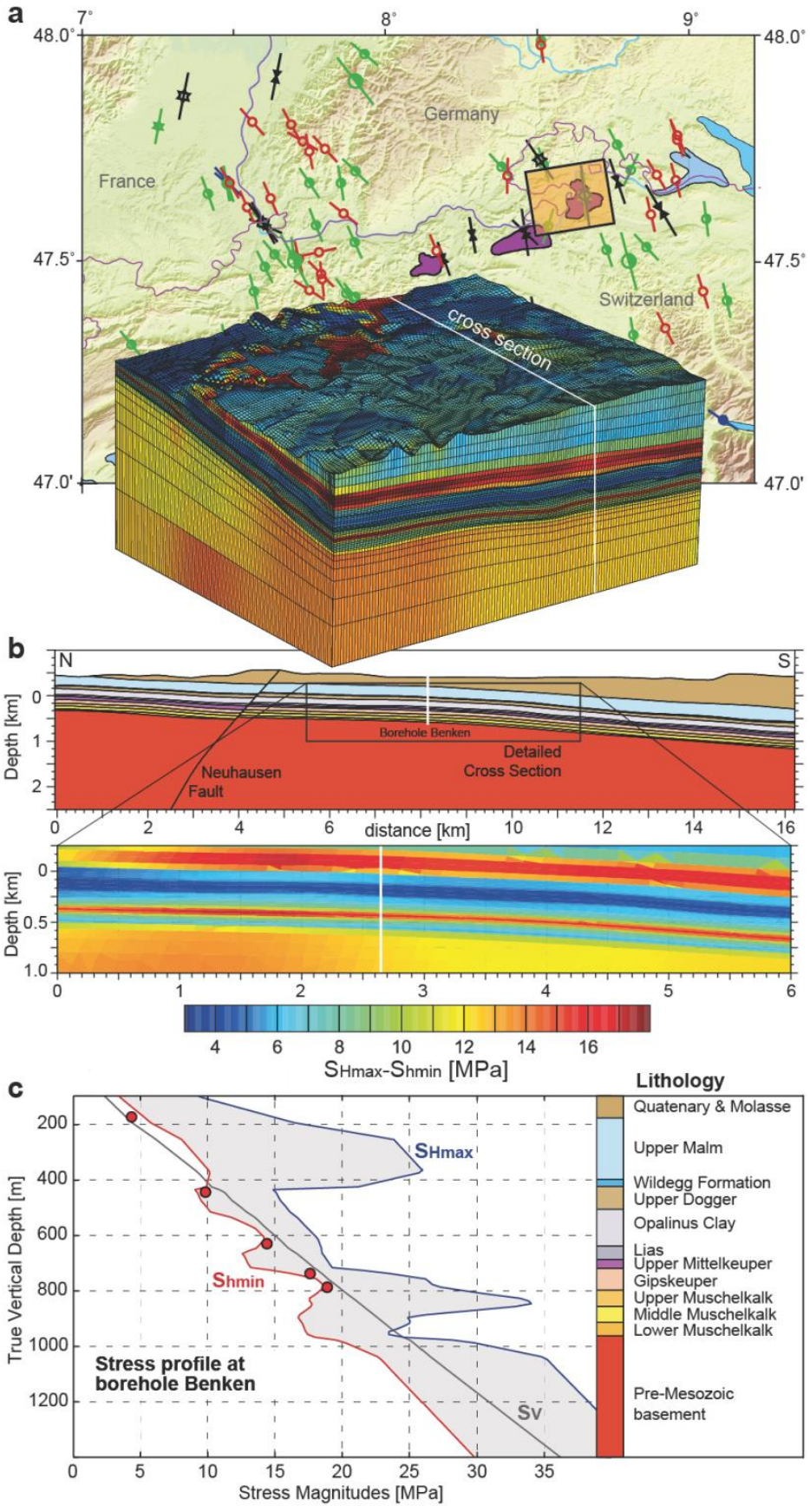

Fig. 7.3: Workflow to deduce a 3D stress field by numerical stress field modelling starting with WSM point data (Ziegler et al, 2020)

8 Local stress variations

There are different sources of stress at different scales which determine the local stress field. Coblentz et al. (2024) distinguish first (> 500 km) and second (100 – 500 km) order stress sources (i.e. large tectonic forces and lateral density variations), third (1-100 km) and fourth (< 1 km) order stress sources (e.g. stiffness contrasts, rock fabric and geological structures).

As already mentioned bevor: significant local stress variations have to be expected, especially in fractured rock masses. Fig. 8.1 and 8.2 illustrate this fact simulating a fracture network inside a block of 10 by 10 m with 4 joint sets, which is characterized by two joint segments located at the lower left corner, with stiffness 10 time lower than for all the other joint segments (all other parameter are identical). The primary stress applied vertical and horizontal at the outer boundary is 5 and 3 MPa, respectively. The local stress disturbance becomes visible in Fig. 8.1 (right) and Fig. 8.2.

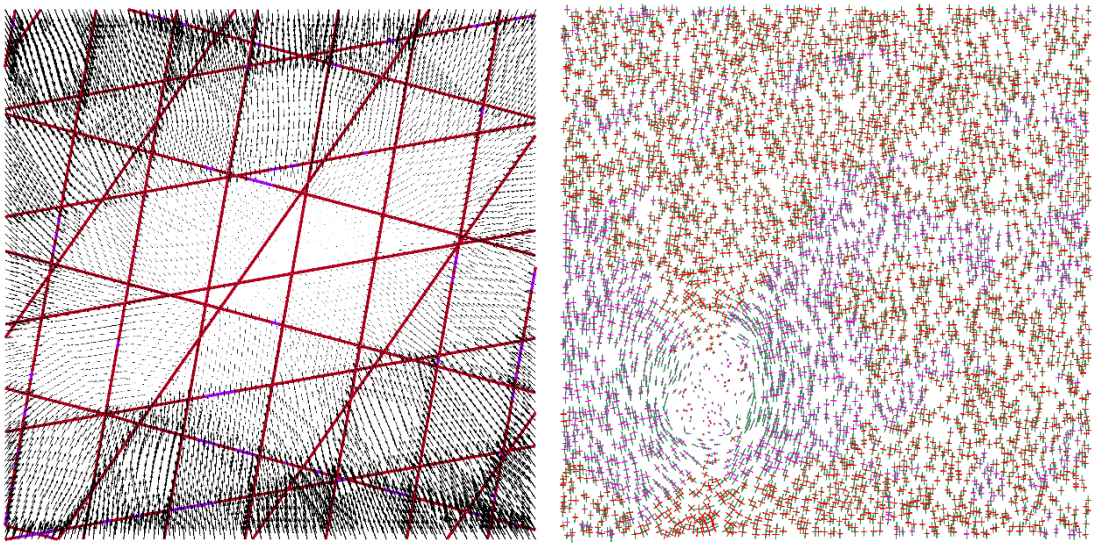

Fig. 8.1: Rock mass with 4 joint sets: left: displacement field, right: principal stresses.

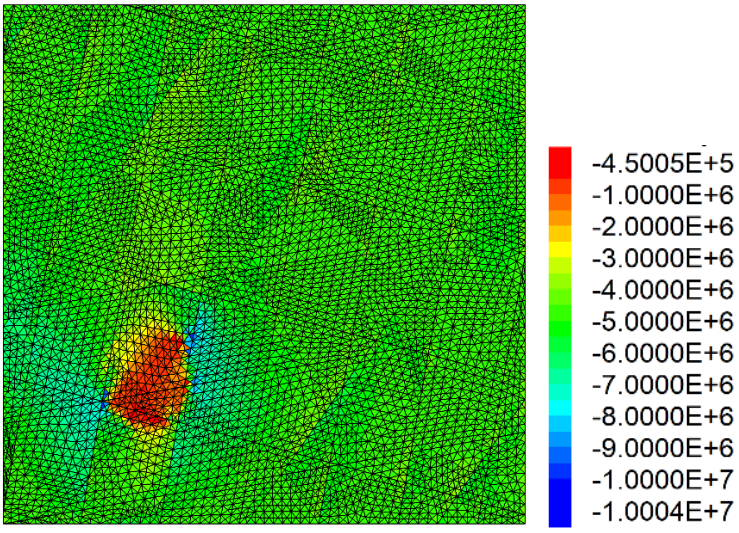

Fig. 8.2: Contour plot of maximum principal stress [Pa] according to Fig. 8.1 (Note: compressive stresses have negative sign).

The same holds for complex fracture pattern like observed in nature and illustrated in Fig. 8.3, which shows the local stress disturbance as Euclidian distance between local stress tensor and mean stress tensor. Fig. 8.3 shows 5 different fracture networks under 3 different states of stress. Higher stress anisotropy lead to slip and tensile failure at the joints, which produces stress redistributions and disturbances, respectively.

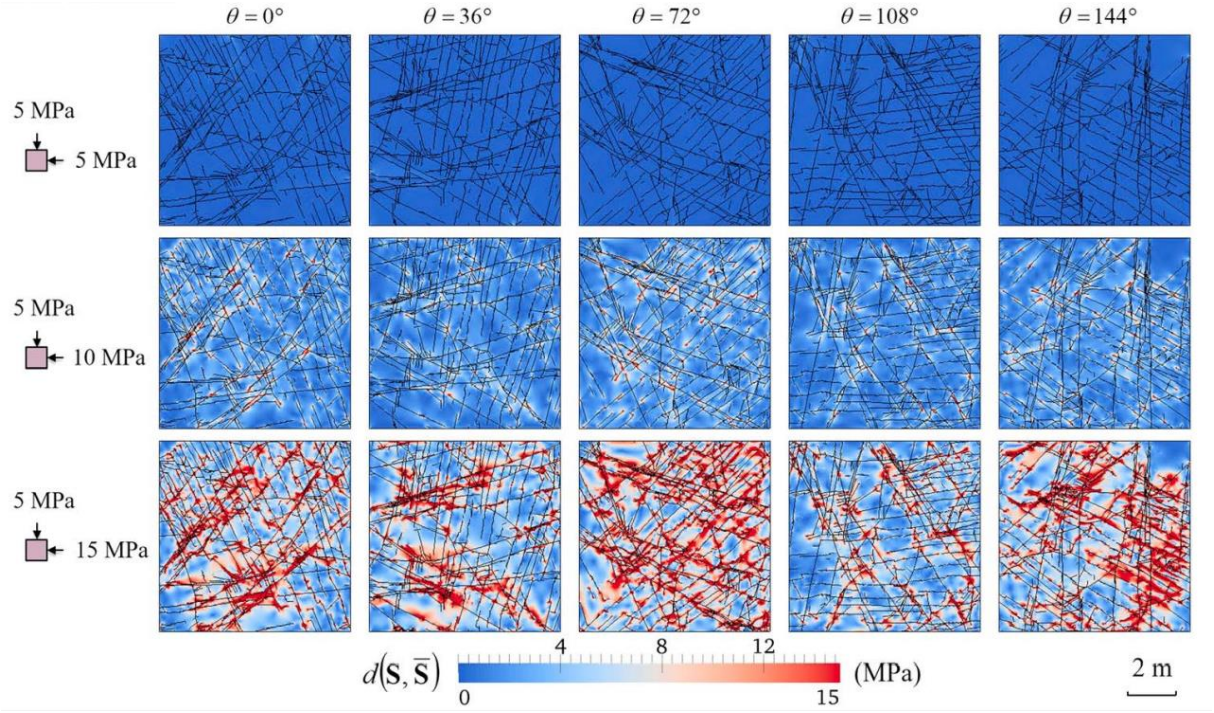

Fig. 8.3: Distribution of local stress disturbance in a natural fracture network using a friction coefficient of 0.6 and different far-field stresses (Lei & Gao, 2018).

9 New methods to determine stress fields at larger scale

Stress fields and especially stress field changes in time can be deduced by high precision measurements of displacements via InSAR data. Another technique – especially in respect to determine the stress anisotropy - is based on measuring changes in elastic wave velocity by evaluating earth tidal strain cycles. Find further explanations in Coblentz et al. (2024).

10 Literature

Anderson, E.M. (1951): The dynamic of faulting and dyke formation with application to Britain, Oliver and Boyd, Edinburgh, 206p.

Braun, R. (2014): RACOS 3D in situ stress analysis. www.dr-roland-braun.com/DE/procedures/racos/index_racos.html, last accessed: 25.08.2020

Byerlee, J.D. (1978): Friction of rock, *Pure Appl. Geophys*, 116: 615-626

Christiansson, R. & Hudson, J.A. (2003): ISRM suggested methods for rock stress estimation – part 4: quality control for rock stress estimation, *IJRMMSci*, 40(7-8): 1021-1025

Coblentz, D. et al. (2024): Characterization, Prediction and Modelling of Crustal Present-Day In-Situ Stresses. Geological Society, London, Special Publications, 546, 47–68

Haimson, B.C. & Cornet, F.H. (2003): ISRM suggested methods for rock stress estimation – part 3: hydraulic fracturing (HF) and/or hydraulic testing of pre-existing fractures (HTPF), *IJRMMSci*, 40(7-8): 1011-1020

Hakala, M., Hudson, J.A. & Christiansson, R. (2003): Quality control of overcoring stress measurement data, *IJRMMSci*, 40(7-8): 1141-1159

Hakala, M.; Christiansson, R.; Martin, D.; Siren, T. & Kemppainen, K. (2013): In situ stress measurement with the new LVDT cell – method description and verification, POSIVA 12-43, Finland

Heidbach, O.; Custodio, S.; Kingdon, A.; Mariucci, M.T.; Montone, P.; Müller, B.; Pierdominici, S.; Rajabi, M.; Reinecker, J.; Reiter, K.; Tingay, M.; Williams, J. & Ziegler, M. (2016): Stress Map of the Mediterranean and Central Europe 2016, GFZ Data Service

Hudson, J.A.; Cornet, F. & Christiansson, R. (2003): ISRM suggested methods for rock stress estimation – part 1: strategy for rock stress estimation, *IJRMMSci*, 40(7-8): 991-998

Konietzky, H. (2005): Numerical stress field modelling for underground structures, in: F. Rummel (ed.): *Rock mechanics with emphasis on stress*, Oxford & IBH Publishing Co. Pvt. Ltd, New Dehli, 55-80

Konietzky, H. & Rummel, F. (2004): In situ stress field measurements and stress field modelling, 2nd Colloquium Rock Mechanics - Theory and Practice*, Mitteilungen für Ingenieurgeologie und Geomechanik der TU Wien*, 6: 46-54

Konietzky, H.; te Kamp, L.; Hammer, H. & Niedermeyer, S. (2001): Numerical modelling of in situ stress conditions as an aid in route selection for rail tunnels in complex geological formations in South Germany, *Computers and Geotechnics*, 28(6-7): 495-516

Konietzky, H. & Blümling, P. (1995): In situ stress field in the Wellenberg area, *Nagra Bulletin* 26: 38-47

Lei, Q., Gao, K. (2018): Correlation between fracture network properties and stress variability in geological media, Geophys. Res. Letters, 45: 3994-4006

Ljunggren, C.; Chang, Y.; Janson, T. & Christiansson, R. (2003): An overview of rock stress measurement methods, *IJRMMSci*, 40(7): 975-989

Reinecker, J.; Tingay, M. & Müller, B. (2003): Borehole breakout analysis from four-arm caliper logs, Guidelines: Four-arm Caliper Logs, World Stress Map Project

Reiter, K.; Heidbach, O.; Müller, B.; Reinecker, J. & Röckel, T. (2016): Spannungs-karte Deutschland 2016

Schmitt, D.R.; Currie, C.A. & Zhang, L. (2012): Crustal stress determination from boreholes and and rock cores: Fundamental principles, *Tectonophysics*, 580(10): 1-26

Sjöberg, J.; Christiansson, R. & Hudson, J.A. (2003): ISRM suggested methods for rock stress estimation – part 2: overcoring methods, *IJRMMSci*., 40: 999-1010

Stephansson, O.; Zang, A. (2012): ISRM suggested methods for rock stress estima-tion – part 5: establishing a model for the in situ stress at a given site, *Rock Mech. Rock Eng.*, 45: 955-969

Tan, X. & Konietzky, H. (2014): Numerical study of variation in Biot's coefficient with respect to microstructure of rocks, *Tectonophysics*, 610: 159-171

Waclawik, P. et al. (2016): Determination of stress state in rock mass using strain gauge probes CCBO, Procedia Engineering, 149: 544-552

Zang, A. & Stephansson, O. (2010): Stress field of the earth's crust, Springer, 322 p.

Ziegler, M.; Heidbach, O.; Morawitz, S. & Reiter, K. (2020): From point-wise stress data to a continuous description of the undisturbed 3D stress field, *Proc. 49. Geomechanics Colloquium*, Heft 2020-4, Publ. Geotechnical Institute, TU Bergakademie Freiberg, H. Konietzky (ed.): 1-11

Ziegler, M. & Valley, B. (2021). Evaluation of the diametrical core deformation and discing analysis for in-situ stress etsimation and application tot he 3.9 km deep rock core from the Basel geothermal borehole, Switzerland, Rock Mech. Rock Eng., 54: 6511-6532